KfK 5125
April 1994

Material Interactions during Severe LWR Accidents

Summary of Separate-Effects Test Results

W. Hering, P. Hofmann
Institut für Materialforschung
Projekt Nukleare Sicherheitsforschung

Kernforschungszentrum Karlsruhe

Kernforschungszentrum Karlsruhe

Institut für Materialforschung
Projekt Nukleare Sicherheitsforschung

KfK 5125

Material Interactions during Severe LWR Accidents;
Summary of Separate-Effects Test Results

W. Hering, P. Hofmann

Kernforschungszentrum Karlsruhe GmbH, Karlsruhe

Als Manuskript gedruckt

Kernforschungszentrum Karlsruhe GmbH
Postfach 3640, 76021 Karlsruhe

ISSN 0303-4003

Abstract

The results of separate-effects tests performed at the Kernforschungszentrum Karlsruhe (KfK) and at the Japan Atomic Energy Research Institute (JAERI) on "low-temperature" physico-chemical material interactions have been critically reviewed. The range of "low-temperature" material interactions spans between 1200 K and 1690 K, the melting temperatures of stainless steel and Inconel respectively. The following material interaction couples have been examined and compared with data from literature: Ag / Zircaloy, (Ag,In,Cd) / Zircaloy, stainless steel / Zircaloy, Inconel 718 / Zircaloy, B_4C / Zircaloy and B_4C / stainless steel. In addition the experimental procedures and the results have been compared. The reaction kinetics generally obey parabolic rate laws indicating that the basic process is a diffusion controlled. The temperature dependence of the reaction rates can be described by Arrhenius equations.

The chemical interactions between Ag/Zircaloy and (Ag,In,Cd)/Zircaloy are controlled by diffusion of Zr into the liquid phase, which is about two orders of magnitude faster than the diffusion coefficient of Ag in solid Zircaloy.

The stainless steel /Zircaloy and the Inconel / Zircaloy reaction rates measured at KfK and JAERI show some differences at temperatures below 1373 K, which can be explained by different contact conditions between the Zircaloy crucible and the stainless steel or Inconel discs and rods, respectively. At temperatures above 1473 K the crucibles at KfK were liquified, whereas at JAERI isothermal tests could be performed up to 1573 K, probably due to the higher Zircaloy mass of the crucibles. The kinetics of both types of interactions are mainly controlled by diffusion of Zr into the liquid mixtures, which form as a result of eutectic interactions; but the diffusion of Fe and Ni in the solid Zircaloy cannot be neglected.

The chemical interactions of B_4C, the BWR absorber material, are investigated in the reaction couples B_4C/Zircaloy and B_4C/stainless steel. Both sets of reaction rates (KfK, JAERI) are comparable and show nearly the same liquefaction temperatures.

In addition, the influence of thin oxide layers on Zircaloy surfaces (10-100μm) were investigated. Generally, the oxide layers delay the onset of the chemical interactions and shift the liquefaction to higher temperatures. Below 45 μm thick oxide layers the KfK and JAERI results are comparable and can be explained by oxygen diffusion from ZrO_2 into β-Zircaloy until the ZrO_2 has been dissolved completely. At higher oxide layer thicknesses the porosity of the ZrO_2 allows some penetration of Fe, Ni, and Zr, so that the time delay does not increase with increasing oxide layer thickness as observed below 45 μm.

Materialwechselwirkungen während eines schweren LWR-Störfalles
Zusammenfassung der Ergebnisse von Einzeleffektuntersuchungen

Kurzfassung

Die Ergebnisse von Einzeleffektuntersuchungen von physikalisch-chemischen "Nieder-Temperatur"-Materialwechselwirkungen, die am Kernforschungszentrum Karlsruhe (KfK) und am Japan Atomic Energy Research Institute (JAERI) durchgeführt wurden, sind kritisch überprüft worden. Der "Nieder-Temperatur"-Bereich erstreckt sich von 1200 K bis 1690 K, der Schmelztemperatur von Edelstahl und Inconel. Die folgenden Materialkombinationen wurden untersucht und mit Literaturwerten verglichen: Ag / Zircaloy, (Ag,In,Cd) / Zircaloy, Edelstahl / Zircaloy, Inconel 718 / Zircaloy, B_4C / Zircaloy und B_4C / Edelstahl. Ferner wurden die experimentellen Methoden gegenübergestellt. Die Reaktionen verlaufen nach einem parabolischen Zeitgesetz, ein Hinweis, daß es sich um Diffusionsprozesse handelt. Die Temperaturabhängigkeit der Reaktionsraten kann durch eine Arrhenius Gleichung beschrieben werden.

Die chemischen Wechselwirkungen von Ag/Zircaloy und (Ag,In,Cd)/Zircaloy werden durch Diffusion von Zr in die flüssige Phase bestimmt, die etwa zwei Größenordnungen schneller ist als die Diffusion von Ag in festem Zircaloy.

Die in den KfK- und JAERI-Experimenten gemessenen Reaktionsraten von Edelstahl / Zircaloy und Inconel / Zircaloy zeigen unterhalb von 1373 K gewisse Differenzen, die auf unterschiedliche Kontaktbedingungen zwischen dem Zircaloy-Tiegel und den Edelstahl- oder Inconel-Scheiben bzw. -Rundstäben zurückgeführt werden können. Oberhalb von 1473 K verflüssigen sich die Tiegel in den KfK-Experimenten, während bei JAERI isotherme Versuche bis ca. 1573 K durchgeführt werden konnten, offenbar aufgrund der größeren Zircaloy-Masse der Tiegel. Die Reaktionskinetik der beiden Wechselwirkungstypen wird hauptsächlich durch die Diffusion von Zr in die flüssige Phase bestimmt, die sich aufgrund der eutektischen Wechselwirkung bildet; die Diffusion von Fe und Ni im festen Zircaloy kann jedoch nicht vernachlässigt werden.

Die chemischen Wechselwirkungen des SWR-Absorbermaterials B_4C wurden in den Materialpaarungen B_4C / Zircaloy und B_4C / Edelstahl untersucht. Die Ergebnisse der KfK- und JAERI-Experimente sind vergleichbar und zeigen fast dieselben Verflüssigungstemperaturen.

Zusätzlich wurde der Einfluß von dünnen Oxydschichten auf dem Zircaloy (10-100µm) untersucht. Im allgemeinen verzögern die Oxydschichten den Beginn der chemischen Wechselwirkung und verschieben die Verflüssigung zu höheren Temperaturen. Unterhalb von ca. 45 µm Schichtdicke sind die KfK- und JAERI-Ergebnisse vergleichbar. Die Verzögerungszeit kann allein durch die Sauerstoffdiffusion vom ZrO_2 ins metallische β-Zircaloy bis zur vollständigen Auflösung des ZrO_2 erklärt werden. Bei höheren Oxydschichtdicken erlaubt die zunehmende Porosität der Oxydschicht eine gewisse Durchdringung von Fe, Ni und Zr, so daß die Verzögerungszeit nicht mehr mit zunehmender Oxydschichtdicke ansteigt wie unterhalb von 45 µm.

Table of Contents

1. INTRODUCTION

As part of the post-accident analysis of the partial core-meltdown accident at TMI-2 a great number of integral experiments have been performed to investigate the physico-chemical material phenomena and processes during a severe fuel damage (SFD) accident /1/. Within the reactor safety research program "Projekt Nukleare Sicherheitsforschung" (PSF) at the Kernforschungszentrum Karlsruhe (KfK) extensive separate-effects tests were performed as a part of the CORA program.

The state of common understanding of the different material behavior processes documented in /1/, defines some areas which are not yet completely understood. One of these areas is the influence of the early-phase core melt formation on the further damage and melt progression within a bundle or a core. The early-phase melt phenomena include liquefaction of fuel rod cladding, Inconel spacer grids, stainless steel tubes of the control rods, and control rod alloy (absorber alloy) due to eutectic interactions.

The CORA early-phase core melt progression experimental program is focused on the investigation of material behavior phenomena /2/ to provide a database necessary for model and code system development and verification /3/. Analyses of the global behavior of fuel elements have been performed, based on measurements of the fluid composition (steam and argon), temperatures of the heated and unheated rods and spacer grids, internal fuel rod pressures, and material relocations during the tests as well as axial material redistribution, changes in the bundle cross-section, hydrogen generation, and oxidation state after test /4,5/. The results indicate that eutectic interactions do initiate or trigger low-temperature early-phase melt progression in a fuel rod bundle due to the formation and release of liquid materials.

To explain the different chemical compositions of various reaction products, formed by chemical interactions between stainless steel (SS) / Zircaloy[1] (Zry), Inconel[2]/ Zircaloy or (Ag,In,Cd) / Zircaloy B_4C / SS, and B_4C / Zry , found in CORA experiments /6,7/ as well as in material examinations of core bore specimens taken from the degraded TMI-2 reactor core /8/, separate-effects tests were performed at KfK and the Japan Atomic Energy Research Institute (JAERI). To investigate the influence of thin oxide layers on the Zircaloy surface, pre-oxidized Zircaloy was used in addition to as-received material.

The first aim of this report is to compare the different results obtained by KfK with those from JAERI and to explain apparent discrepancies in some experimental results. The main aims, however, are to identify common mechanism of these chemical interactions and to describe the

[1] ZIRCALOY is a trademark of Westinghouse Electric Company, Pittsburg, PA. In this report Zircaloy-4 is meant.
[2] INCONEL is a trademark of the INCONEL Corporation, USA. In this report Inconel-718 is meant.

influence of thin oxide layers on the Zircaloy cladding surfaces on the chemical interactions. Finally recommendations are given on how this data base should be used for model development and verification.

2. MATERIAL INTERACTIONS DURING SFD-ACCIDENTS

Severe reactor accidents can be divided into several phases depending on temperature and boundary conditions in the core and the primary cooling system. To investigate the material behavior phenomena and processes during these phases integral bundle test were performed in-pile as well as out-of-pile /1/. The most significant phases of a severe accident will be illustrated using an integral out-of-pile test, which was performed in the CORA test facility (s. Figure 1 /6/). The CORA bundle tests were well instrumented to obtain all data necessary for the explanation of the phenomena and the physico-chemical material processes observed /1,2/. As an example, the pressurised water reactor (PWR) specific test CORA-13 was choosen, which was also selected by the OECD/ CSNI as an International Standard Problem (ISP-31) /6/.

The experimental results of the test CORA-13 are summarized in one test-sequence diagram (s. Figure 2 /3/), which allows a precise reconstruction of the time-dependent test history of the bundle. The diagram is composed of three parts representing the most significant phases of the test. It starts at 3000 s with the initial heat-up phase and ends with the quench-phase, which is magnified for better resolution.

In the upper part of the diagram the phenomena occuring in an axial test-section length of 1.2 m are represented as a function of time. The temperatures are given as temperature front (TF) lines derived from the thermocouple measurements of the heated rods (dashed lines, indicated by S). The TF-lines indicate in the vertical direction the axial temperature gradient at any time between 3000 s and 5050s and in the horizontal direction the temperature histoty at any axial elevation between 0.0 m and 1.20 m. Furthermore, local temperatures measured at grid spacer locations are marked (upper Zircaloy spacer grid: Z, Inconel spacer grid: I), to demonstrate their thermal response during heat-up.

Cladding failure derived from the measured internal rod pressure history (dotted area) and the bundle melt progression observed as melt release and relocation in the video films (dashed area) are also shown in Figure 2. The bundle melt progression shows many details which would complicate this picture too much, so that only the first and the last phenomena are indicated. At the lower end of this part, the melt drainage into the water pool obtained by analysis of thermocouple readings near the water level in the quench tank (s. Figure 2) is shown by droplet symbols.

The center part of Figure 2 gives the fluid composition at the lower end of the bundle. Here, the time delay caused by mixing of steam in the Ar carrier gas after 3300 s in the large cavities of the steam generator system is taken into account, as well as evaporated water from the quench tank (Figure 1). At temperatures beyond 1500 K (see upper part) the Zircaloy/steam reaction produces large quantities of hydrogen, especially during the quench process. The mass flux of

hydrogen measured in the off-gas system is represented by the dashed area. Moreover, the electric bundle power ramp (P_{el}) is shown (dashed-dotted line).

Combining all the data in Figure 2, the axial and temporal locations of the phenomena observed can be given for each test-phase. The sequence of phenomena, listed in the lower part of Figure 2, allows a classification of the recognized effects concerning their influence on the damage initiation and damage progression (local or global), which is valid for all PWR-specific CORA tests.

The phases indicated in Figure 2 are chosen by temperature and experimental conditions (shut down of electrical power starts the cool-down phase) . For material interactions the escalation phase must be split into a phase of low-temperature interactions (s. section 2.2) and one of high-temperature interactions (s. section 2.3). This split is rather uniform in the axial direction as can be seen in the TF-lines of Figure 2. The TF-line of 1773 K approximately indicates the beginning of the high temperature phase with melting of stainless steel and Inconel, as indicated in Figure 3.

2.1. THERMOHYDRAULIC PHASE

If in a nuclear reactor design basis accident the heat sinks or the heat transport mechanisms (forced or natural convection) fail, the temperatures in the core increase and the evaporation of the water results in uncovering of the upper part of the core. In the remaining water as well as in the two phase region above, low temperatures are maintained, whereas in the dry or superheated steam region above the water level rapid temperature increase of the fuel rods occurs. Assuming adiabatic boundary conditions for the fuel elements an average heat-up rate of 1 K/s is estimated, which was used as a guidance for the performance of most of the CORA tests.

Therefore, the heat-up phase indicated in Figure 2 is the end of the thermohydraulic phase of a SFD accident, leading to temperatures which allow the melting of PWR control rod material (Ag, In, Cd; indicated by the 1073 K TF-line) and ballooning or collapsing of the cladding tubes. Up to the end of the thermohydraulic phase ($T < 1200$ K) only the beginning of the oxidation of Zircaloy and stainless steel has to be considered.

For accident management measures, this phase has the largest potential for delaying the heat-up of the core which leads to temperatures above 1500 K and to subsequent core damage and possibly also core meltdown.

2.2. LOW-TEMPERATURE MATERIAL INTERACTIONS

The range of physico-chemical material interactions and the formation of liquid phases covers more than 2000 K, starting at around 1000 K with the melting of (Ag,In,Cd) alloy and ending with the melting of UO_2 at about 3000K. The interval of low-temperature material interactions spans up to 1750 K, the liquidus temperatures of stainless steel and Inconel (s. Figure 3). In Figure 3 the chemical material interactions and the formation of liquid phases are shown on the left side. In the center part, the processes occurring during a PWR SFD accident for a control rod are given as a function of temperature and initial pressure ratio (bottom). The behavior of the fuel rods, however, is much more complicated, so that it is divided into mechanical , physical and chemical behavior. At the left side of Figure 3 typical time scales calculated from the initial heat-up rates (min: 0.2 K/s max.: 1 K/s) are outlined. The corresponding reaction kinetics of the indicated chemical interactions are summarized in Figure 4, which gives an overview of the reaction kinetics of the low- and high temperature material interactions /2,15,21,26,31/.

In detail Figure 3 shows schematically the influence of individual processes on the global course of a SFD accident during early phase melt relocation up to the formation of ceramic (U-Zr-O) melts. As can be seen easily, low-temperature material interactions strongly influence the integral behavior of the bundle by formation of predominantly metallic melts.

From the isothermal section of the ternary phase diagram Fe-Ni-Zr /8, 9/ and the relevant binary phase diagrams of Fe-Zr or Ni-Zr /10/, the lowest eutectic temperature is found in the Fe-Zr system at about 1200 K on the zirconium rich side. This temperature is exceeded in the center of the bundle after 3800 s and in the lower third between 3900 s and 4100 s as can be seen in Figure 2. With respect to the physical state of the reaction components (bundle or core elements) three types of interactions can be distinguished (s. Figure 3):

1. **Solid - gaseous reactions at the interface bundle components-fluid:**
   - Oxidation and embrittlement of Zircaloy in a steam atmosphere,
   - Oxidation of stainless steel and Inconel, and
   - Hydrogen dissolved in metallic Zircaloy (below 1200 K /12/)
     (so far not observed in CORA fuel rod bundles).

2. **Solid - solid chemical interactions :**
   These only take place as long as no liquid phases in the reaction zone appear, for example due to eutectic interactions:
   - Inconel springs in spacer grids with the Zircaloy of the cladding tubes,
   - BWR control rod material (B_4C) in contact with the stainless steel tubes,

- Beginning of fuel dissolution due to interaction with Zry cladding,
- Stainless steel of the PWR control rod cladding with the Zircaloy of the control rod guide tube.

3. **Solid - liquid chemical interactions:**

- PWR control rod material (80 wt% Ag, 15 wt% In, 5 wt% Cd /11,14,15/) with the Zircaloy of the cladding surface after failure of the stainless steel cladding of the control rod,
- BWR absorber material (B_4C) and stainless steel mixtures (B_4C+SS) with the Zircaloy of the canister walls and adjacent fuel rods.

A change from solid-solid interactions to solid-liquid interactions can sometimes be detected by a sudden increase of the reaction rates, as observed in the B_4C/Zry system (s. Figure 8) /31/. The interactions and the reaction kinetics are discussed in section 4 in detail.

Low-temperature material interactions result in the formation of a metallic melt. The uranium concentrations in the stainless steel-Zircaloy and Inconel-Zircaloy melts are negligible as long as solid Zry protects the UO_2 pellets from being attacked by the melt. If such metallic melts remain in the hot zone of a bundle, they will be transformed into ceramic phases by steam oxidation of (Fe,Cr,Zr). The lowest liquefaction temperature of the eutectic material interactions is exceeded at around 3900 s at app. 0.9 m elevation (see Figure 2).

In CORA-13 the failure of the fuel rod cladding was indicated at app. 4100 s by a drop of the internal rod pressure from 0.45 MPa to system pressure (0.22 MPa). The initial internal rod pressure was kept low to avoid clad ballooning. From the video films, however, first melts were observed earlier, as rivulets at 4080 s at 0.8m and as droplets at 0.4 m bundle elevation. No identification of the origin of the melts was possible. This indicates that the interaction between stainless steel and Zry at the control rods has perforated the Zry guide tube wall earlier than the interaction between Inconel and Zry at the upper grid spacer at app. 0.85 m.

Though material thicknesses and interaction kinetics are of the same order of magnitude, the differences in the axial temperature distribution inside the bundle (given by the TF-lines between 3900 s and 4100 s) have to be considered too. Also, it can be assumed that no large protective oxide layer has been formed on the inner surface of the Zry guide tube, retarding the onset of interaction. Further on, the internal pressures of the fuel rods and the simulators, as well as those of the control rods and the system pressure influence the burst times /3/. Considering all these uncertainties, including the errors in the temperature measurements, only one conclusion can be given: the two independent concurrent processes lead to perforation of the cladding tubes in the same time period but at different elevations and temperatures.

From the axial bundle temperature profiles the axial location of the perforation of the guide tubes is located at 0.95 ± 0.1 m, whereas the fuel rod claddings fail at the upper Zircaloy spacer location at 0.88±0.02 m bundle elevation.

After release, the molten (Ag,In,Cd) PWR absorber alloy comes into contact with the cladding surfaces of the adjacent fuel rods. The subsequent interactions between the control rod alloy and the fuel rod cladding cannot be observed directly. To identify and locate results of the material interactions, metallurgical post-test examinations of bundle cross-sections at elevations where relocated material is present are necessary. Here the observation of the mass of the adherent material as well as its chemical composition are helpful in understanding the physical and chemical phenomena which take place.

During the time required for the perforation of the cladding its temperature is increased up to 1773 K, so that melting of metallic bundle components (stainless steel and Inconel) is a simultaneous process. As can be seen, the heat-up rate limits the dissolution time, so that in this case a clear separation between the different processes cannot be obtained by the global analysis. Metallurgical analyses of the reaction products, however, cannot distinguish between the processes, because the subsequent high temperatures during the test transient (s. Figure 2) destroy the initially formed eutectic interaction products.

2.3. HIGH-TEMPERATURE MATERIAL INTERACTIONS

In Figure 3 the boundary between the high- and low-temperature phase is arbitrarily defined as the melting point of stainless steel, the maximum temperature considered for low-temperature material interactions. The high-temperature material interactions end at around 3000 K, above which only melting of all initial materials or reaction products takes place. Above 1773 K the material interactions are strongly accelerated by the fast heat-up (about 10 K/s) due to the exothermic Zircaloy oxidation by steam, starting at around 1500 K. If enough oxygen from the steam environment is available all metallic surfaces or melts which have been released after cladding failure, will be covered with oxide layers at these temperatures.

The main reactions in the reactor core to be considered are:

1. Oxidation of Zircaloy and stainless steel by steam,
2. Fuel dissolution by molten Zircaloy in contact with the UO_2 pellets,
3. Interaction between disintegrated and /or partially dissolved UO_2 and molten Zircaloy forming a metallic (U-Zr-O) melt with ceramic precipitations at higher temperatures /2/,
4. Eutectic reaction between α-Zr(O) and ZrO_2, and
5. Oxidation of the fuel by steam, and

6. Oxidation of the B_4C by steam.

Furthermore, at high temperatures melting of remaining core components or reaction products can occur:

7. B_4C, Al_2O_3 (burnable poison rods in some US PWRs), and
8. ZrO_2, and UO_2.

In the CORA-13 test, reactions 1 to 5 are found, the other phenomena cannot occur because these materials were not present (5, 6) or the temperature did not reach the melting points (7, 8). The melts formed during this period have mostly a ceramic character.

As can be seen by the TF-lines in Figure 2, these material interactions took place up to 4100 s in the upper third of the bundle. The heat transport by relocating melts with subsequent solidification increases the temperatures in the lower third of the fuel rod bundle, which remained rather cold due to the enhanced convective cooling /3/, so that these high-temperature interactions can occur only down to 0.15 m bundle elevation. Due to failure of the thermocouples after 4700 s in the lower half of the bundle, no temperature information is available on cool-down, but it can be assumed that the temperatures remain above 1773 K up to the beginning of the quench phase.

During the quench phase a secondary renewed heat-up is detected for a short period of time between 0.7 m and 1.0 m bundle elevation indicating that there was sufficient metallic material left, though protected by oxide layers. The thermal shock of the materials induced by the two-phase liquid above the flooding front (water) cracks the protective oxide layers creating fresh metallic surfaces, which will be oxidized immediately by steam.

The short time period at high temperature, less than 30 s above 2273 K, give some hints about the amount of metal which remaind for further oxidation. Generally, two processes stop finally the oxidation, cool-down below 1200 K and the lack of metallic Zircaloy. For example, above 0.9 m bundle elevation the oxidation is stopped earlier, as the temperature drops due to the quench front reaching this bundle elevation. This may indicate, that rather than a complete consumption of the metallic Zr, the sudden temperature decrease has stopped the oxidation.

Generally, the large amount of hydrogen produced in the quench phase can be explained by the sudden increase of the metallic surface at high temperature, due to crack formation in the protective ZrO_2 layer and the subsequent oxidation by steam.

3. RESULTS OF SEPARATE-EFFECTS TESTS

The short overview of the early phase melt progression phenomena in a PWR fuel rod bundle or core indicates that the processes leading to damage of fuel rods are the failure of control rods, the release of absorber alloy (Ag, In, Cd), and the subsequent chemical attack of the Zircaloy fuel rod claddings by the ejected absorber alloy. Therefore, these chemical interactions have to be investigated in detail. The reaction kinetics have been examined in separate-effects tests in Germany (KfK) and Japan (JAERI). For all investigations the zirconium alloy used was Zircaloy-4 (Zry) and the nickel-based alloy Inconel 718 (Inconel).

3.1. EXPERIMENTAL SETUP

At the Institut für Materialforschung (IMF) of the Kernforschungszentrum Karlsruhe (KfK) isothermal annealing experiments were performed in a high temperature muffle furnace which provides an isothermal environment, so that the small reaction samples do not experience any temperature gradient /13,14,15,21,26,31/. All test configurations show similar cylindrical arrangements as can be seen in Figure 5a (left), except for the liquid-solid separate-effects tests performed at JAERI (s. Figure 5a right) /15/.

At the Department of Fuels Reliability Laboratory of the Japan Atomic Energy Research Institute (JAERI) experiments were performed below 1473 K in an resistance furnace and above up to 1953 K in an infrared-mirror furnace shown in Figure 5b . Here the samples are inserted in a quartz crucible, which is encapsulated by tantalum cladding which acts as a radiation receiver (s. Figure 5b). A surrounding quartz tube protects the four heater pins. The atmosphere, inert or oxidizing (steam), is controlled by flow-meters. The main heat transport mechanism is radiation amongst the four heater pins, the tantalum cladding, and the crucibles or test materials.

In the separate-effects tests typical heat-up rates are about 5 - 10 K/s. The cool-down rates depend on the stored (latent) heat and the cooling conditions. Depending on the temperature the annealing times vary from one to several hundred minutes.

3.2. POST-TEST INVESTIGATIONS

After the test, the samples were mechanically cut, grinded, polished and analyzed by an optical microscope. The extend of the interaction zone has been measured at several positions to obtain the minimum, maximum and the average thicknesses of the remaining materials. Though the interaction zone is often not planar and varies circumferentially the average value is appropriate to define the kinetics. With respect to perforation, however, the maximum value gives the minimum

time required to dissolve a given thickness of Zircaloy and can be used as a conservative approach.

Moreover, special reaction zones of interest were examined by a scanning electron microscope (SEM) with an energy dispersive X-ray (EDX) system to obtain the detailed structure and the morphology of the interaction zone and the spatial distribution of the elements. The latter information is very useful to determine the most significant reactions between the components of the investigated material couples. The shape of the interfaces gives some hints about the basic diffusion processes leading partially to liquifaction due to eutectic reactions.

3.3. INVESTIGATED SYSTEMS

3.3.1. Absorber Alloy (Ag,In,Cd) / Zircaloy

The absorber alloy of PWR control rods is the material with the lowest melting point ($T_m \approx 1073$ K) in a LWR core. The (Ag,In,Cd) alloy is kept in its stainless steel cladding until this fails (s. Figure 3). Later, when released under high internal pressure (low system pressure) after mechanical or chemical failure of the stainless steel cladding and the Zircaloy guide tube the interaction with the cladding of adjacent fuel rods becomes interesting. Liquid control rod material relocating down the fuel rod cladding causes chemical interactions which are assumed to be the processes initiating cladding failure and subsequent flowering /5/.

Generally, all separate-effects tests performed at KfK /14,15/ and JAERI /16-18/ show that the reaction kinetics of the chemical interactions (Ag, In, Cd)/Zry and Ag/Zry lead a rapid dissolution of the Zircaloy by the liquid. The reaction rates are listed in Table 2.

At KfK the liquid control rod alloy (Ag,In,Cd) is kept in a Zircaloy crucible of 6 mm inner diameter with a 2 mm thick wall which is closed gas-tight by a conical Zircaloy plug (s. Figure 5a). At JAERI a Zircaloy disc is immersed in the liquid alloy, which is kept in a quartz crucible as can be seen on the right side Figure 5a. In both cases the ratio of interface surface and liquid volume is comparable, but at KfK the initial mass of Zircaloy is twice as high. At temperatures near the melting point of the absorber alloy (low overheating) saturation along the solid-liquid interface can occur for long annealing times.

The annealing capsules at JAERI allow evaporation of the cadmium (app. 0.1 MPa at 1500 K), so that a reduction of the Cd content in the absorber alloy cannot be excluded for long annealing times and/or high temperatures. Quantitative data of the concentration of Ag, In, Cd, and Zr in the solidified liquid after the test are not available. In real SFD accidents the early released control rod alloy still has the initial composition, whereas after some time the Cd content will be decreased /18/ so that the liquid alloy is mainly composed of Ag and In.

To compare the results of the different test series the measured reaction rates (x^2/t) and the correlations obtained from the experimental data are plotted versus the reciprocal temperature in Figure 6. The Arrhenius plots show the reduction of the Zircaloy wall or disc thickness due to the dissolution in the molten Ag or (Ag,In,Cd) absorber alloy. The two upper solid lines reflect the interaction between liquid absorber alloy and Zircaloy. Between the experimental results of KfK and JAERI no pronounced difference can be observed . The data are completely within the error bands.

For comparison the interaction between liquid Ag and Zircaloy is also shown (dotted line). A larger difference in the reaction kinetics is found between the (Ag,In,Cd) / Zry and the Ag / Zry interaction systems. The deviation is large at lower temperatures and levels out near liquifaction temperature at about 1500 K, this behavior will be discussed in section 4.1.2.

Moreover, at KfK the (Ag,In,Cd) / pre-oxidized Zry interaction was examined using a Zircaloy crucible with an initial ZrO_2 layer of 10 µm thickness (dashed line). A different behavior is seen comparing the results obtained with a protective thin oxide layer with those obtained from as-received materials. The reaction rates are about one order of magnitude smaller. The reaction rates given here $x^2/(t-t_0)$ do not account for the "incubation time" t_0 necessary to convert the protective ZrO_2 layer into an α-Zr(O) layer. The basic processes are discussed in section 4.2.1 in detail.

The results are consistent with each other, as can be seen in Table 2 and Table 6. The influence of the In and Cd on the dissolution, however, has to be checked in detail (see section 4.1.2).

3.3.2. *Stainless Steel / Zircaloy*

In PWR's each control rod is composed of a Zircaloy guide tube in which a stainless steel tube containing the absorber alloy (Ag, In, Cd) is inserted. The stainless steel / Zircaloy interaction occurs at the contact positions between the outer surface of the control rod cladding and the inner surface of the guide tube. As already pointed out the ratio between inner pressure (hydrostatic and vapor pressure) and system pressure influences the contact pressure in radial direction (s. Figure 3). Also after perforation of the claddings the axial and radial relocation of the molten control rod alloy is dominated by this pressure ratio, until the whole amount of the liquid control rod alloy above the location of the breach is released.

At KfK stainless steel (AISI 316) rods are pressed into a Zircaloy crucible (s. Figure 5a) so that, due to the smaller thermal expansion of Zircaloy, a good solid-state contact is established at higher temperatures /15,23/.

The same geometrical arrangement is used at JAERI /20/ (s. Figure 5a) but here stainless steel AISI 304 instead of AISI 316 was used (see section 4.1.3.). Furthermore, the crucible walls were 3 mm thick and the initial Zry mass was nearly twice as high. An annular gap of 50 μm separates both species in the radial direction at room temperature. No information about the real contact conditions at temperature is available, but from the individual thermal expansion coefficients /13/ it can be calculated that the annular gap should have disappeared by around 1330 K.

After the test in all cases a nearly homogenous interaction layer is found, which was liquid at temperature. The decrease of the stainless steel rod diameter (dashed lines) and Zircaloy (solid lines) wall thicknesses were measured. The results obtained at KfK are indicated by dark lines, whereas those of JAERI are drawn as light grey ones (s. Figure 7). Both materials participate to different extents in the chemical interactions. Within the error band of the experiments both sets of results are comparable, even taken into account the different chemical compositions of the stainless steel alloys (316, 304). The measurements at 1523 K made by JAERI have to be checked because no solid stainless steel remained to be measured. One possible reason is the higher Zry inventory leading to a complete liquifaction of the stainless steel at around 1473 K. The correlations obtained from these data are nearly parallel indicating that no change in the basic interaction process occurs between 1273 K and 1573 K. A list of the reaction rates is given in Table 3.

For comparison the results of isothermal diffusion-bonding experiments /23/ at 1373 K between stainless steel 304 and Zircaloy are outlined in Figure 7 as single symbols (+,o). The slightly higher reaction rates can be explained by the good solid state contact, which was achieved by polished surfaces and good positioning of both materials using a spring load during annealing time.

In addition, the influence of a initial thin oxide layer (≤ 50 μm) on the Zircaloy surface is investigated. The results (s. Figure 13) will be discussed in section 4.2 in comparison with those of the reaction couples (Ag,In,Cd) / Zircaloy (s. Figure 6) and Inconel / Zircaloy (s. Figure 14).

3.3.3. *Inconel 718 / Zircaloy*

All fuel rods of a LWR fuel element (FE) are fixed laterally by grid spacers, which are mounted at app. 0.5 m to 0.7 m distances along the rods. Two types of spacer grids are used: pure Inconel spacers and Zircaloy spacers with springs made of Inconel 718 or another nickel-based alloy. So the local areas of interaction are well defined and it only depends on the local temperature, which can be obtained from the axial temperature profile, whether or not interaction starts.

In the CORA tests the Inconel / Zry interaction leads to perforation of the fuel rod cladding at around 1500 K releasing the fill gas as noticed in the internal pressure recordings. From the axial

temperature gradient it can be deduced that the upper Zircaloy spacer is the first of the three spacers in the CORA bundles which exceeds 1230 K (s. Figure 2).

In Figure 8 the temperature dependence of the reaction rates in Inconel (dashed lines) and in the Zircaloy (solid lines) are given (s. Table 4). Both materials participate e.g. are consumed to different extents in the chemical interactions. The experimental results obtained at KfK are indicated by light grey lines /25, 26/, whereas those obtained by JAERI /27, 28/ are drawn by black ones. The activation energies for the reaction rate of the Zry attack are nearly the same up to app. 1423 K. The difference in the reaction rates is within the experimental accuracy, as can be seen by the single points. At app. 1440 K, however, a sudden increase (jump) of one order of magnitude is detected for the JAERI data, which may be correlated with the formation of a liquid phase (an eutectic at the Zr-rich side of the binary Ni-Zr phase diagram). This behavior was not observed in KfK experiments.

The reaction rates for Inconel are about one order of magnitude smaller. Up to 1373 K the results of both sets of experiments fit very well, the activation energy differs only slightly. Above this temperature, no data from the dissolution of the Inconel are available, due to its complete liquifaction. A complete list of the measured reaction rates is given in Table 4.

Except for the increase of the reaction rates discussed above, the kinetics of this system are comparable with the interaction system stainless steel/Zircaloy and are discussed in section 4.1.3. Also the influence of an initial oxide layer on the Zircaloy is analyzed and compared with results obtained from the other interaction systems. The results coincide with measurements at 1273 K /29/.

Separate-effects tests with real geometries were also performed at JAERI /28/, using a representative segment of an Inconel spacer grid and LWR fuel rod cladding. Without an initial protective oxide layer on the cladding the well-known structure of the reaction zone was observed: a small layer adjacent to the Inconel (51 μm) with an enriched Cr content and a much larger layer in Zircaloy (330 μm, 1248 K, 900s in Ar), liquid at temperature.

Tests performed in pure oxygen revealed no interaction below 1473 K. Above this temperature the onset of the reaction was observed to be retarded, while the oxidation of the Zircaloy continues. The thicknesses of the oxide layers obtained are calculated by phenomenological equations to 10-20 μm on the uncovered surface of the tube cladding /30/. At the contact area it is assumed that no oxide layer has formed. The observed behavior correlates with results obtained earlier /24/.

In the real geometry, however, the molten materials are not kept at place, so that the liquid can relocate axially and laterally. The liquid increases the contact area so that parts outside the initial contact area can be partially dissolved too.

3.3.4. B_4C / Stainless Steel and B_4C / Zircaloy

In BWR's the control rod is composed of four blades forming a cross. Each blade is composed of numerous small stainless steel tubes containing boron carbide powder. In axial direction, the powder is kept in place by stainless steel bullets, which are crimped within the stainless steel tube of the control rod. The control rod failure is initiated by the interaction between boron carbide and stainless steel.

Direct contact to the adjacent flow channel walls of the fuel elements (canister) made of Zircaloy is possible due to bowing of the absorber blades at higher temperatures or after failure of support structures. From integral tests it is known that also molten stainless steel - boron carbide (B_4C) mixtures can interact with the Zircaloy of adjacent fuel rod channel (canister) walls. In case of bowing a solid-state contact is established.

The two interaction systems B_4C/stainless steel and B_4C/Zry are therefore discussed together in this section. So far results of separate-effects tests (s. Figure 9) are available for B_4C/SS 316 from KfK /31/, for B_4C/SS 304 from JAERI /30/, and for B_4C/Zry from KfK /31/ and JAERI /30, 32/. A complete list of the reaction rates is given in Table 5.

Furthermore, at JAERI the interaction behavior of B_4C powder (solid grey line) was compared with that of B_4C pellets (short dashed line), which were used in liquid metal fast breeder reactors, but no significant difference in the reaction kinetics could be observed. The chemical interaction only allows the measurement of the decrease of the Zry wall thickness or stainless steel discs directly. Another method would be the determination of concentration profiles across the interaction zone. The interaction zone shows some layered structures which are discussed in /31,33/.

In the B_4C/stainless steel system reaction rates are available from KfK (long dashed lines) up to 1523 K and from JAERI up to 1623 K (s. Figure 9). Up to app. 1300 K the KfK results are below those obtained at JAERI. The original KfK correlation was steeper, indicating a slightly higher activation energy compared to the results of JAERI, in the same manner as observed in the stainless steel Zircaloy system (s. section 3.3.2). Theoretical consideration indicated that the results of the B_4C/Zry interaction have to be checked again /33/, neglecting the results at the lowest temperature (1073 K) and including those of 1573 K. The corresponding correlation is shown as the thin dash-dotted line which is nearly equal to the latest experimental result obtained by JAERI /32/.

Around 1500 K a jump of the reaction rates for the system B_4C/stainless steel of more than two orders of magnitude is noticed which can be explained by a liquifaction of the B_4C /stainless steel interaction layer shortcutting the diffusion path. One possible reason why this behavior was not observed at KfK may be the different mass ratio and will be discussed in detail in /33/.

A detailed discussion of both interaction systems will be performed in section 4.1.4.

4. DISCUSSION

The experimental results obtained from the separate-effects tests performed so far are classified and compared with respect to the type and the kinetics of the interactions. Furthermore the relevant chemical processes will be discussed. The reaction kinetics of the investigated chemical interactions generally show a parabolic behavior of the interface movement, indicating that the basic process should be a diffusive mass transport either in the solid or in the liquid phase(s).

A liquid phase is present from the beginning for the Ag/Zry and the absorber alloy (Ag,In,Cd)/ Zry interactions or formed during interaction due to eutectic reactions (SS/Zry, Inconel/Zry). The general temperature dependence obtained from results of various isothermal separate-effects tests reveal that the basic processes are thermally activated and can be described by Arrhenius correlations.

4.1. INTERACTIONS WITH AS-RECEIVED ZIRCALOY

The interaction between (Ag,In,Cd) and Zircaloy seems to be dominated by diffusion of either Ag, In, and Cd into the solid Zircaloy or by Zr in the liquid absorber alloy. To avoid problems associated with the required quaternary phase diagram to extract the exact boundary concentration, the simpler system Ag/Zr is discussed first, which was investigated at JAERI /18/.

4.1.1. Ag / Zry

In the binary system Ag/Zr two diffusion processes have to be taken into account: 1. solid state diffusion of Ag in the Zry and 2. diffusion of Zr in the liquid Ag. Between 1200 K and 1500 K the diffusion coefficient of Ag in solid β-Zry is in the order of the self-diffusion of Zr /35/: $10^{-13} < D_{Ag} < 10^{-12}$ m²/s /35/, two orders of magnitude lager than in α-Zr at 1117 K /37/. The diffusion process in the liquid is effected by the physical and thermodynamical properties of the liquid and can be estimated using a semi-phenomenological correlation based on measurements and microscopic theory (the liquid is assumed to be composed of rigid spheres) /36/:

$$D_{eff}^{Tm} = 3.27*10^{-10}*\left(\frac{T_m}{M}\right)^{1/2} * V^{1/3}, \frac{m^2}{s}, \qquad (1)$$

with M the molar mass, V the molar volume and T_m the melting temperature of Ag (T_m=1234 K). Using the data published in /36/ a self-diffusion coefficient for Ag is calculated to $D_{Ag} = 3*10^{-9}$ m^2/s, which can be assumed as an upper limit for the diffusion coefficient of Zr in liquid Ag. Since this value is more than three orders of magnitude larger than those in solid Zr, the diffusion of Ag into the solid Zr can be neglected henceforth.

A more sophisticated approach is to calculate the diffusion coefficients from the reaction rates measured in the separate-effects tests and from the boundary concentrations extracted from the binary phase diagram of Ag-Zr. A solution of the diffusion problem can be assumed, if the characteristic diffusion length L of the chemical interactions is small (L < 0.2 * H) compared to the dimension of the sample (H) vertical to the interface. Than the concentration changes are negligible for |x| > L, as illustrated in the schematics below.

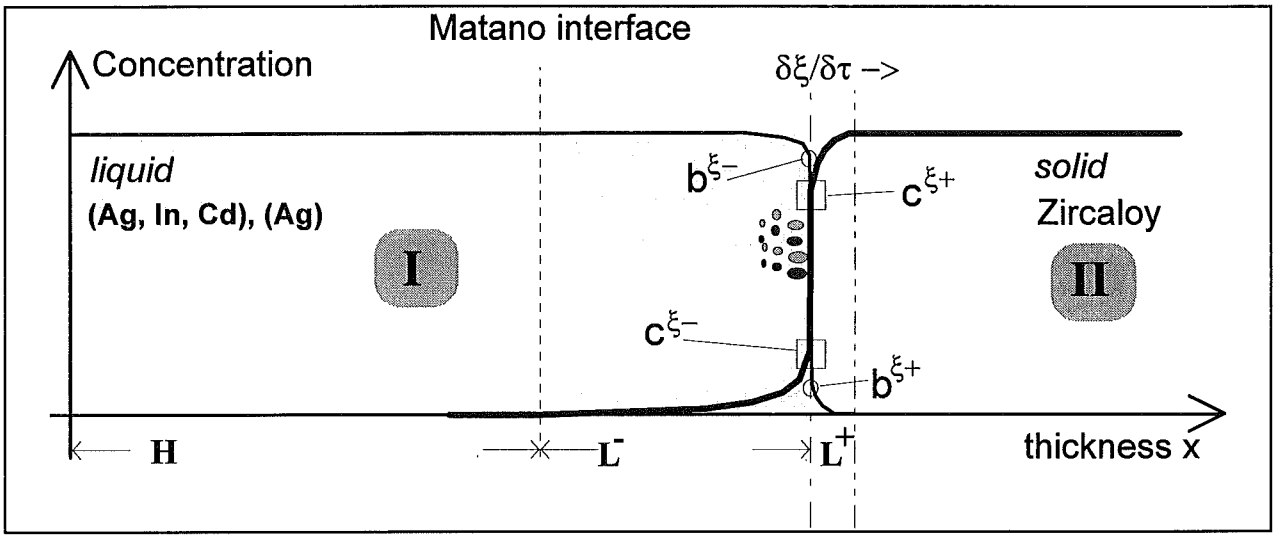

Schematics of the liquid/solid interaction (Ag, In, Cd)/Zry or Ag/Zry with the initial interface ("Matano interface"). The boundary concentrations of Zr are indicated by **c** , those of Ag by **b**.

Next the Stefan problem for the moving boundary with fixed boundary concentrations $c^{\xi-}$, $c^{\xi+}$ has to be solved for the diffusion coefficients of Zr from the measured reaction rates k_p.

$$\frac{d\xi}{dt} = \frac{1}{\Delta c_\xi} * \left(D^I_{Zr} * \frac{dc^I}{dx} - D^{II}_{Zr} * \frac{dc^{II}}{dx} \right), \frac{m}{s}, \qquad (2)$$

with $\Delta c = c\xi+ - c^{\xi-}$ the concentration jump of Zr at ξ, and D' and D'' the diffusion coefficients of Zr in liquid Ag and in solid β-Zry. Since the diffusion coefficient in the liquid is more than three orders of magnitude larger than that in the solid state (s. Table 13), Eq. (2) can be simplified as follows:

$$\frac{d\xi}{dt} = \frac{1}{\Delta c_\xi} * \left(D^I_{Zr} * \frac{dc^I}{dx} \right), \frac{m}{s}. \qquad (3)$$

So the concentration gradient dc^I/dx on the liquid side of the interface at ξ can be estimated using the characteristic length L:

$$\frac{dc^I}{dx} \propto \frac{\Delta c^I}{\Delta x} \propto \frac{\Delta c^I}{L} \propto \frac{\Delta c^I}{\sqrt{D^I * t}} \quad ,$$

with $\Delta c^I = c_\xi - c_{(L)}$, the bulk concentration in the liquid (here $c_{(L)} = 0.0$). Than Eq. (3) can be integrated to :

$$\xi \propto \frac{\Delta c^I}{\Delta c_\xi} * 2 * \sqrt{D^I_{Zr} * t} \quad , \tag{4}$$

The effective diffusion coefficient of Zr in liquid Ag is then given as a function of the boundary position ξ after the annealing time t which is assumed to be short ($t \ll \xi^2/D$):

$$D^I_{Zr} \propto \frac{\xi^2}{4*t} * \left(\frac{\Delta c^I}{\Delta c_\xi}\right)^2 \quad , \frac{m^2}{s} \quad , \tag{5}$$

or as a function of the measured reaction rates $k_p = \xi^2/t$:

$$D^I_{Zr} \propto \frac{k_p}{4} * \left(\frac{\Delta c^I}{\Delta c_\xi}\right)^2 , \frac{m^2}{s} \quad . \tag{6}$$

As a first approach the diffusion coefficients are estimated using the minimum, the average, and the maximum reaction rates measured at JAERI /18/ and the boundary concentrations from the binary phase diagram at ξ /11/. The values obtained in the temperature range between 1273 K and 1473 K are within the range of: $8*10^{-11} < D_{Zr} < 9*10^{-10}$ m²/s. Due to this first approach based on experimental data the diffusion values given in Table 9 may differ from the exact values by one order of magnitude.

The estimated diffusion coefficients are one order of magnitude smaller than the self-diffusion of liquid Ag but more than two orders of magnitude larger than the self-diffusion of Zr and more than three orders of magnitude larger than the diffusion of Ag in solid Zr. Even if diffusion along grain boundaries or sub granular boundaries is taken into account /35/ this large difference is only reduced by a factor of three.

As indicated by the cool-down temperature curves measured at JAERI, the increasing Zr content influences the liquefaction and solidification temperatures of the alloy. Depending on annealing time, reaction species and temperature, various stagnation points can be found during cool-down, indicating various solidification temperatures of the different phases in the liquid alloy.

For a precise calculation of the diffusion coefficients the solubility of Zr in Ag has to be considered more carefully. For higher Zr concentrations in the liquid the estimation discussed above fails because a concentration-dependent diffusion coefficient D(T,c) is required (see Eq. 7).

4.1.2. *(Ag,In,Cd) / Zry*

For a sufficient description of the (Ag,In,Cd)/Zr interaction the diffusion coefficient of Zr and the corresponding boundary concentrations are required. Therefore the SEM-WDX results between 1273 K and 1423 K (s. Table 10) are reviewed indicating the existence of mainly three phases in the vicinity of the solid-liquid interface (< 0.5 mm) as can be seen in Table 10 A. Except for one phase the Cd concentrations are less than 1 at%. Though no Zr is found in this phase the influence of Cd on the chemical interaction can be neglected, so that a ternary phase diagram of Ag-In-Zr is sufficient to describe the (Ag,In,Cd)/Zr interaction. The indicated "phase type" in Table 10 only expresses the optical impression due to the grey value.

In section B of Table 10 the relevant concentration of the boundary layer is given. The concentrations behave as expected; the Zr concentration rises with temperature and reaction time so that they are used to determine the diffusion coefficients D_{Zr} in the liquid absorber alloy. The values estimated by Eq. (6) are in the order of 10^{-11} m²/s for 1273 K and 1373 K (s. Table 11), somewhat smaller than those obtained from the minimum reaction rates of Ag/Zr interaction (s. Table 9).

From tracer diffusion measurements in solid Ag-Zr alloys with various Ag contents /19/ diffusion coefficients D_{Zr} were measured between 10^{-13} up to 10^{-12} m²/s between 1200 K and 1500 K. The diffusion processes at Ag concentrations above 8 at% Ag dissolved in Zr were not investigated. The additional influence of In can also not be estimated. Therefore, no recommendation for the diffusion coefficient in the liquid can be given.

Since the concentration values are obtained at single points, averaging was performed neglecting the Cd concentration (s. Table 10, C) along a line parallel to the interface at a distance of app. $(D_{Zr}*t)^{1/2}$. The results indicate that an integral analysis is required since the visual integration can only distinguish between different grey levels and not between chemical compositions.

For a more appropriate solution of this diffusion problem, measurements of the diffusion coefficient and boundary concentrations are necessary for various Zr and In concentrations. The temperature and concentration dependence of the diffusion coefficient can be determined. From the literature the concentration dependence of the diffusion coefficients can be described as /19/:

$$D^{I}_{Zr}(c_{Ag},T) = D_0 * \exp\left(-Q/RT\right) * \exp\left(\alpha/T^2\right), \qquad (7)$$

where α describes the unknown concentration dependence of diffusion coefficient.

So far, no reliable diffusion data for Zr in (Ag,In,Cd) could be measured so that for model development and verification, the measured reaction rates have to be used since no phase change takes place above 1200 K in the (Ag,In,Cd)/Zry system. Both sets of reaction rates (KfK or JAERI)

can be used, if the solubility limit of Zr in the alloy is checked by the solidus lines of the ternary Ag-In-Zr phase diagram.

4.1.3. Iron-Nickel Alloys / Zircaloy

In this section the results of two interaction systems, the stainless steel / Zry (s. Figure 7) and Inconel / Zry (s. Figure 8), will be dicussed togehter because both systems are iron-nickel alloys and the reaction kinetics are similar. As already pointed out, the main diffusion processes in both systems takes place in the liquid formed due to the eutectic reactions above 1200K. Furthermore Fe and Ni are known as ultra-fast diffusers (together with Co /36, 38/) associated with small ionic radii (<0.1nm) allowing fast interstitial movements in the bcc lattice of β-Zry /35, 39/. The third element of the alloys, chromium, has a lower mobility than Fe or Ni (one order of magnitude above self diffusion of Zr /35/), so that its influence on the reaction kinetics can be neglected henceforth, because it enriches at the boundary adjacent to the stainless steel or Inconel /21/.

Chemical composition:

Zircaloy (Zry) :		1.5 wt% Sn, < 0.2 % Fe, > 0.07 % Cr, < 0.1 % Ni
Stainless steel:	(AISI 316):	18 wt% Cr, 14 % Ni, 2.5 % Mo, balance Fe
	(AISI 304):	20 wt% Cr, 11 % Ni, no Mo, balance Fe
Inconel 718:		53.4 wt% Ni, 18 % Fe, 17.9 % Cr, 3.1 % Mo,

Both alloys, stainless steel (SS 304 and SS 316), are composed of Fe and Ni of various concentrations, allowing the formation of ternary interaction products such as (Fe, Ni) Zr_2, as indicated in the isothermal section of the ternary phase diagram Fe-Ni-Zr (s. Figure 12). Therefore, the chemical compositions of the alloys are idealized to clarify the most significant diffusion process.

Idealized chemical composition:

Zircaloy:	**100 wt% Zr**
Stainless steel:	**80 wt% Fe,** 18 % Cr, 2 % Mo
Inconel 718:	**72 wt% Ni**, 18 % Cr, 3 % Mo, ...

The two stainless steel alloys have nearly the same chemical composition except for Mo which is only present in the AISI 316 type, to enhance the corrosion resistance against acids.

At temperature the Zircaloy has a bcc-lattice (β-Zry) in which the diffusion coefficients of Fe and Ni are somewhat smaller (s. Table 13) compared the hcp of the α-Zry /35/, but nevertheless two orders of magnitude larger than the self-diffusion coefficients of Zr /38, 39/.

In both chemical systems diffusion layers are formed at both sides of the initial Matano interface, forming three different layers. In the liquid layer (I) diffusion coefficients are unknown whereas in the two layers in the solid state (II and III) the diffusion coefficients are known from the literature. The layer I is liquid above 1200 K (Fe-Zr) and 1233 K (Ni-Zr) respectively, due to the eutectic reactions at the Zr-rich side of the binary systems (s. Figure 12), so that for all temperatures discussed herein two solid-liquid interfaces c and ξ have to be taken into account.

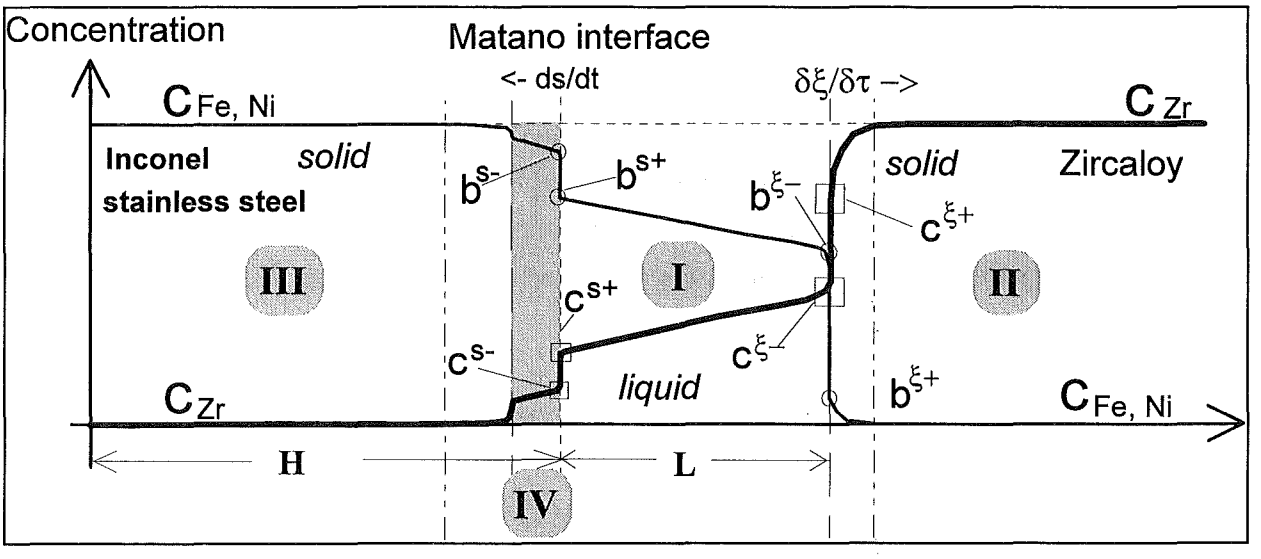

Schematics of the liquid / solid interaction (Iron-Nickel) / Zircaloy at 1218 K < T < 1600 K with one liquid reaction layer (I) and three solid ones in the Zircaloy (II), in the stainless steel or Inconel (III), and adjacent to the Iron-Nickel alloy (IV) in which the chromium is enriched. The boundary concentrations of Zr are indicated by **c**, those of Fe or Ni by **b**.

In this paper, only the order of magnitude of the diffusion in the liquid layer I will be estimated based on the experimental results. A detailed theoretical analysis which considers all processes in the four layers is under way elsewhere and will be published soon /27/. From the ternary phase diagram (s. Figure 11) it can be seen that the deviations between the tie lines of both reaction couples and the relevant binary systems at the boundary are small but not negligible so that the concentrations given by the binary phase diagrams can be used only for a first estimation.

The movement of the phase boundaries are controlled by diffusion of Fe, Ni from layer (III) through (IV) to (I) and of Zr from layer (II) to (I). The diffusion of Zr into the solid layer (III) can be neglected since the solubility is < 1 at% (s. Figure 11). The diffusion coefficients of Zr in SS or Inconel (III) are comparable with the self-diffusion coefficient, so that the movement of this interface is controlled by the diffusion coefficient of Fe and/or Ni in the liquid and their

boundary concentrations in layer I. Moreover, the diffusing materials have to penetrate the layer IV in which chromium is enriched.

At the other interface the diffusion of Fe and Ni into the Zry cannot be neglected, since their diffusion coefficients are of the same order of magnitude as the expected diffusion of Zr, D^I_{Zr} in the liquid. From section 4.1.1 the diffusion coefficient in the liquid D^I_{Zr} is known to be in the order of 10^{-10} m²/s at around 1273 K and from Table 13 $D^I_{Fe,Ni}$ is found to be in the order of 10^{-11} m²/s (at 1200 K).

For a first approach based on the experimental results and using the values from Table 13 diffusion coefficients for D^I_{Zr} were estimated in the order of $6*10^{-11}$ to $4*10^{-9}$ m²/s for the Fe/Zr system and to $2*10^{-9}$ to $3*10^{-10}$ m²/s for the Ni/Zr system in the temperature interval between 1273 K and 1473 K (see Table 14). Though the temperature dependence and the boundary concentrations are not well known in the latter case (Ni/Zr) a more detailed investigation is necessary, which is beyond the scope of this review.

The theoretical considerations, however, can help to discuss the experimental findings in detail and to determine the most reliable experimental results.

4.1.3.1. Stainless steel / Zircaloy

As estimated, the diffusion of Zr in the liquid reaction layer dominates the reaction kinetics of the interface adjacent to the Zircaloy if no saturation occurs in the liquid. A closer look to the temperature dependence shown in Figure 7 reveals that some kind of saturation may have occurred in JAERI's test capsules above 1423 K. Neglecting the reaction rate at 1573 K which is affected by the second eutectic at around 1577 K (0.088 at% Zr), then an increasing deviation from the postulated parabolic behavior can be noticed (thin dotted line).

Since such a behavior was not observed at KfK this can only be explained by a saturation of the liquid, so that the diffusion coefficient and /or the concentration gradient across the liquid is reduced. The lower volume ratio at KfK $V_{Zr}/V_{SS} \approx 2.7$ compared to $V_{Zr}/V_{SS} \approx 5$ at JAERI may have contributed to an earlier consumption (liquefaction) of the stainless steel disc before the Zircaloy crucible is liquefied completely. For a more sophisticated approach the final chemical composition of the liquid is required. Exceeding the eutectic temperature of app. 1570 K a jump in the boundary concentration at the interfaces may lead to a faster movement of the boundary ξ due to the increased Zr transport.

Below 1570 K no change in the reaction system is detected. Therefore the experimental correlations obtained from isothermal experiments can be used as a first approach for model development and verification.

4.1.3.2. Inconel / Zircaloy

The system Inconel / Zircaloy seems to be more complicated as can be seen in the temperature dependence of the reaction rates (s. Figure 8). Below app. 1443 K no significant deviation from parabolic behavior is observed. Above 1373 K the lack of solid Inconel is indicated as observed in the SS/Zry interaction. The jump at 1443 K indicate the same process as discussed for the results at 1573 K in section 4.1.3.1.

The estimated effective diffusion coefficients given in Table 14 do not show the expected temperature dependency. One explanation is that the boundary concentrations depicted from the binary boundary systems of the ternary phase diagram Fe-Ni-Zr do not describe the situation in reality very well. Here only measured concentrations can give the basis for a more detailed explanation and further modelling. As described above, the experimental correlations obtained from isothermal experiments can be used as a first approach.

4.1.4. B_4C / Stainless steel and B_4C / Zircaloy

The slopes of the measured reaction rates are given in Figure 9. The physical and chemical interaction of the two couples are discussed in detail elsewhere /31,33/. Generally the diffusion of B and C into stainless steel or Zircaloy are the rate-controlling processes, creating carbides and borides in the steel or Zircaloy matrix. In both cases ternary phase diagrams are required to explain the observed reaction layers.

The results of the B_4C / Zry interaction (lower solid line at Figure 9) reflect two different thermal activated processes. The lowest eutectic temperature in the equilibrium binary phase diagrams of Zr-B, Zr-C and Zr-$B_{0.5}C_{0.5}$ is around 1888 K, so that the formation of a liquid layer is not supported. Another possible explanation is that the measurement at 1870 K is influenced by the eutectics mentioned above, and the data at 1773 K are still a result of the process determining the kinetics at lower temperatures. Then, neglecting the data at the lowest temperature, the experimental reaction rates can be described by the thin dashed line (s. Figure 9) /27/. A detailed theoretical consideration of the complex B_4C/Zircaloy diffusion processes provided the basis for this approach /33/, which was experimentally confirmed by recent results of JAERI /28/.

The theoretical description of the B_4C/Zircaloy interactions /31/ in the temperature range from 1073 K up to 1773 K is given in /33/. Up to app. 1500 K, only one layer, a two-phase-mixture of ZrB_2 and ZrC is formed, whereas above 1400 K, an additional layer of ZrB_2 appears. The meas-

ured reaction rates, however, can be described very well by only one Arrhenius equation (see Figure 9), so that the rate-determining process should be the same. As was found, the limiting process of the mass transfer through the two-phase region is the diffusion of boron atoms in the ZrB_2 phase. The diffusion coefficient of boron in ZrB_2, which was estimated from interaction experiments between Zr and B, correlates within the limits of the accuracy of the measurements with the observed reaction rates in the B_4C/Zircaloy interaction /33/.

Above app. 1870 K localized liquid phases appear due to eutectic melting in the ternary B-C-Zr system. In this temperature region, the thermodynamic and kinetic data are scarce, so that only supplementary measurements can give hints about the basic processes and their kinetics.

As a result, the correlations obtained from the measured reaction rates can be used within the temperature range mentioned above, because the relevant physical process do not change their character or other processes do not contribute significantly. Also above 1870 K, the measured reaction rates /30, 31/ which are in a good agreement can be used too.

In all cases the mass or volume ratio of both species have to be considered carefully, especially with respect to the use of experimental correlations in integrated code systems for analysis of integral tests or reactor applications.

4.2. INFLUENCE OF AN INITIAL ZRO_2 LAYER ON THE CHEMICAL INTERACTIONS

In all the interaction systems discussed above as-received materials were used; no oxide layer influenced the reaction kinetics of the chemical interactions. However, if a thin oxide layer on the Zircaloy surface prevents the direct contact between the components, a delay of the reaction, called the incubation time, is noticed. This incubation time can be explained as the time necessary for the dissolution of the ZrO_2 layer by diffusion of oxygen from the ZrO_2 into the metal, forming a growing oxygen stabilized α-Zr(O) layer.

According to the experimental observations /21, 26/ the ZrO_{2-x} layer becomes permeable at a certain thickness, so that Fe and Ni, can diffuse through the ZrO_2 into the α-Zr(O). So the first eutectic interaction between (Fe, Ni) and Zr occurs at grain boundaries of the α-Zr(O) layer forming local liquefaction (liquid islands) as depicted in the center part of the schematics below. Due to the oxygen concentration gradient in the α-Zr(O) layer the islands become larger with increasing distance from the ZrO_2 / α-Zr(O) interface (see lower part of the schematics). The end of the incubation time is defined by the onset of the eutectic interaction at the β-Zry / α-Zr(O) interface leading to a liquid (Fe, Ni, Zr) phase. The reaction kinetics in the post incubation period are reduced than those measured in case of a metal / metal reaction couples with no oxide layer, because of the lower mobility of Fe and Ni in the ZrO_2 and the α-Zr(O) layer.

4.2.1. Incubation Period

The incubation times t_0 (see Table 8) shown in Figure 12 for the three investigated reaction couples (Ag,In,Cd)/Zry, SS 316 /Zry, and Inconel 718/Zry were calculated from the measured isothermal reaction rates, which show a parabolic behavior after the incubation time t_0:

$$k_p = \frac{\xi_j^{\,2}}{(t_j - t_o)} \longrightarrow t_o = t_j - \frac{\xi_j^{\,2}}{k_p} \qquad (8)$$

with: k_p the parabolic reaction rate, and ξ_j the layer thicknesses measured in the experiment j after an annealing time $t_j = t+t_0$. Several deviations from the expected behavior can be seen in Figure 12 :

1. The incubation times do not increase as expected with increasing initial oxide layer thicknesses above 20 μm ,
2. above 1450 K, the incubation times for Inconel / pre-oxidized Zry and SS 316 / pre-oxidized Zry decrease faster than below this temperature, and
3. in the case of (Ag,In,Cd) / pre-oxidized Zry, the incubation times are more than one order of magnitude smaller than in the other examined systems.

In the following schematics a possible sequence of intermediate states of the oxide layer dissolution and/or penetration leading to a non-protective remnant oxide layer is shown.

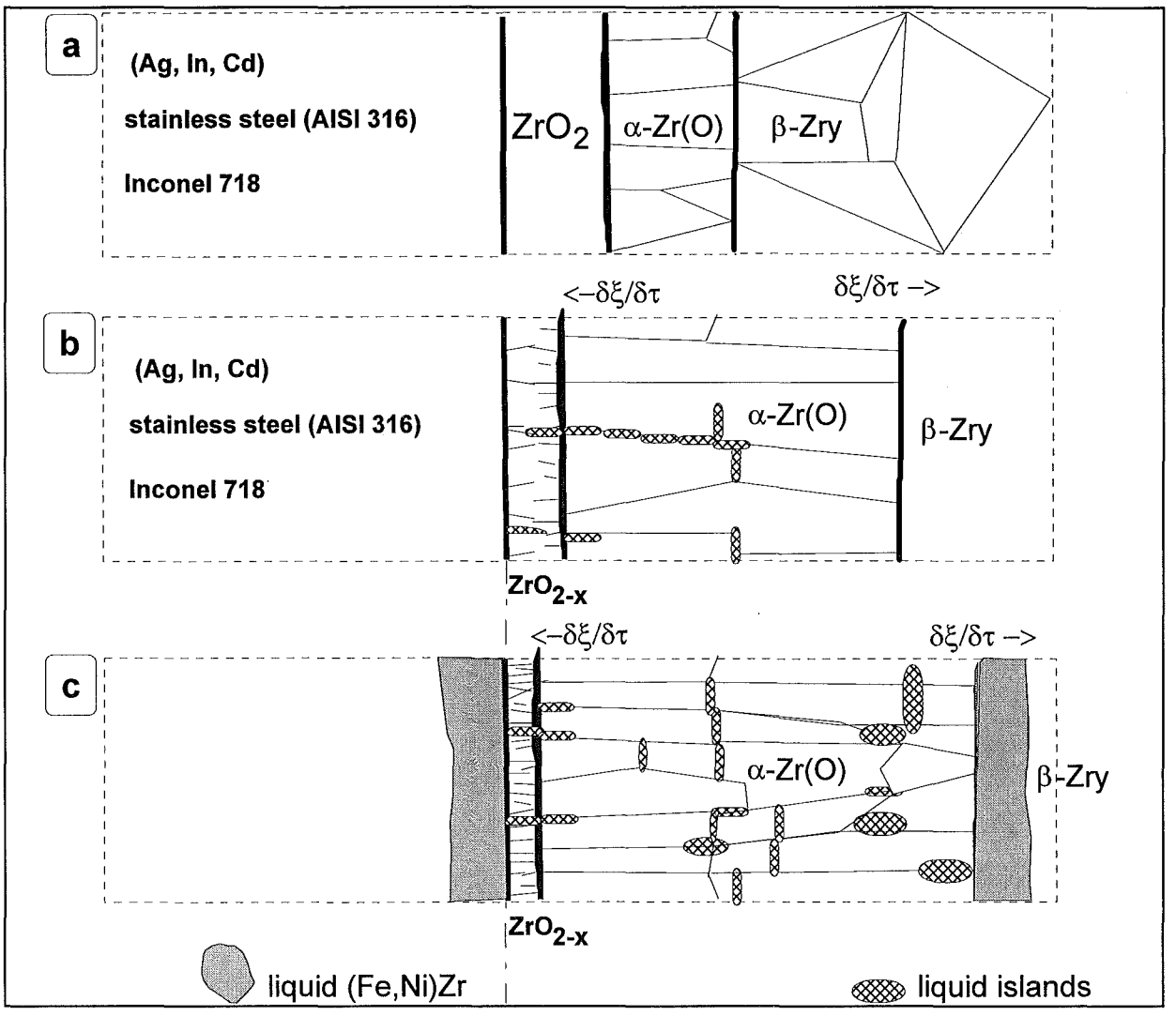

Schematics of the dissolution and penetration of a thin initial oxide layer on the Zircaloy surface:

a. ***initial layer sequence:*** metallic material (liquid or solid), ZrO_2 , α-Zr(O) , (app. same thickness as ZrO_2) and β-Zr,

b. partially dissolved ZrO_2 layer by diffusion of O into the growing α-Zr(O) under the formation of substoichiometric ZrO_{2-x} ;
(Fe,Ni) diffusion through the ZrO_{2-x} , and
eutectic interactions between (Fe,Ni) and Zr at the α-Zr(O) grain boundaries,

c. formation of liquid islands at the α-Zr(O) grain boundaries due to eutectic interaction between (Fe,Ni) and Zr,
formation of a liquid (Fe, Ni, Zr) phase at the α-Zr(O)/β-Zry interface due to Fe and/or Ni penetration through the remnant ZrO_{2-x} and the enlarged α-Zr(O) layer, and
oxygen diffusion from α-Zr(O) into the liquid alloy forming a (Fe,Ni,Zr,O) phase.

These observations cannot be explained if only the oxygen diffusion is taken into account. Other material-dependent processes have to contribute to the observed behavior of the incubation times for oxide layers < 20 μm:

- In the tetragonal oxide (above 1480 K) penetration can occur along defects such as lateral or vertical (to the interface) cracks formed due to tensile stress /43/, grain and/or sub-granular boundaries and/or along oxidized precipitates (Fe, Ni)Zr_2 due to the impurities in the Zircaloy /44/. These processes can lead to non-protective remnant oxide layers.
- Local liquid islands in the α-Zr(O) layer form a short-circuit, so that diffusion in the liquid (Fe, Ni) Zr has to be taken into account as the fastest diffusion process instead of volume diffusion in the α-Zr(O) layer.

The influence of these postulated processes can be estimated from the deviation of the measured incubation times from the idealized ones, which can be calculated from the ZrO_2 dissolution. The calculated incubation time due to oxide dissolution can be estimated neglecting the oxygen diffusion in the ZrO_2 (dc/dx ~ 0). Furthermore the thickness H of the α-Zr(O) is regarded as large compared to the characteristic diffusion length L (see also schematics in section 4.1.1). Then the diffusion coefficient D in α-Zr(O) (see Table 13) and the boundary concentrations at the interface ξ (ZrO_2, α-Zr(O)) c_ξ^+ and c_ξ^- determine the incubation time:

$$t_0 \approx \frac{\delta_{Ox}^2}{4 * D_O^I{}_{\alpha-Zr(O)}} * \left(\frac{\Delta c_\xi}{\Delta c_\alpha} \right)^2 . \qquad (9)$$

with $\Delta c_\xi = \rho * c_\xi^- - c_S^+$ and ρ the Pilling-Bedworth ratio (1.56). With this first approach the incubation times can be estimated to be of the same order as the measured ones. For an improved solution the diffusion of oxygen in the ZrO_2 as well as in the β-Zr has to be taken into account.

From the theory mentioned above the dependence is like δ_{Ox}^2. To fit the experimental data two extensions of the correlation are proposed to take into account the deviation from parabolic behavior. In Eq. (10) the deviation from δ_{Ox}^2 behavior is expressed by a parameter $A^{(0)}$. To account for the observed remnant oxide layers (δ_m), Eq. (11) was used to fit the calculated incubation times (s. Table 8). The "activation energy" Q and the pre-exponential factor $A^{(1)}$ should be of the same order of magnitude for both interaction systems. The results of a non-linear fit is given in Table 12.

$$t_0(\delta_{Ox}, T) = A^{(1)} * \delta_{Ox}^{(2-A^{(0)})} * \exp(Q/RT) , \ s \qquad (10)$$

$$t_0(\delta_{Ox}, T) = A^{(1)} * (\delta_{Ox} - \delta_{rem})^2 * \exp(Q/RT) , \ s \qquad (11)$$

4.2.1.1. (Ag,In,Cd) / Zry

For the system (Ag,In,Cd)/Zry, only the influence of an oxide layer of 10 μm thickness was examined. The measured incubation times are more than one order of magnitude smaller than those obtained from the Inconel/Zry or SS/Zry systems as can be seen from Table 8.

One possible explanation may be the instantaneous liquid-solid contact between the alloy and the ZrO_2 surface above 1073 K. In the experimental procedure the Zry crucible with the control rod alloy is heated up in an tube furnace under flowing argon until the temperature exceeds 1173 K. Then the crucible with the liquid alloy is transferred into the annealing furnace /14/ and when its temperature is 20 K below the desired annealing temperature time measurement was started. For each annealing temperature and species this time is roughly the same, but for the (Ag,In,Cd)/Zry interaction the time of liquid/oxide interaction is increased because the absorber alloy is liquid above app. 1023 K. To determine a correlation of $t_0 = f(\delta_{Ox},T)$ the database is too small.

4.2.1.2. Iron-Nickel Alloy / Zircaloy

As can be seen from Figure 12, at low oxide layer thicknesses (≤ 20 μm) the incubation times correlate very well. Above 45 μm, only the results from the SS 316 / Zry interactions are reliable. The results of the Inconel / Zry interactions show at larger oxide layers even smaller incubation times. Such a behavior cannot be explained except by assuming a very porous oxide structure above 50 μm, so that liquid material can penetrate along them, short-circuiting the oxide layer and creating non-protective remnant ZrO_2 layers.

From the fit of Eq. (10) a value of δ_m is obtained of app. 12 μm, but the pre-exponential factor is very different, indicating different dependencies on the initial oxide layer thickness. Due to the large uncertainties in the measurements and the subsequent calculation of t_0 (s. Table 8), the database is not sufficiently consistent to allow a microscopic interpretation of the results. Nevertheless, for the purposes of integral codes, for each of the investigated reaction couples, a consistent set of parameters can be given, allowing determination of the onset of eutectic reaction.

4.2.2. Post-Incubation Period

In this section, only the measured reaction rates are discussed, the onset of the reactions, however, is delayed by the incubation times given in Table 8 and shown in Figure 12. The relevant reaction rate of the interaction (Ag,In,Cd)/Zry is given as a dashed line in Figure 6, those of SS 316 / Zry in Figure 13, and those of Inconel /Zry in Figure 14.

4.2.2.1. (Ag,In,Cd) / Zry

With a 10 μm initial oxide layer the reaction rates of the (Ag,In,Cd)/Zry interaction do not differ significantly from those measured between as-received materials at low temperatures. Near the liquifaction temperature (app. 1500 K), however, the difference is app. one order of magnitude. In this case the higher stability of α-Zr(O) and the lower diffusion of Zr in this layer are responsible for the reduced reaction kinetics since ZrO_2 is considered to be stable.

4.2.2.2. Stainless steel 316 / Zry

Generally, the reaction rates of the SS 316/Zry interaction (s. Figure 13) are about one order of magnitude smaller than those measured between as-received materials (s. Figure 7), but the temperature dependence is nearly the same, showing slightly different behavior above and below app. 1480 K. Such a behavior may be associated with the phase transition in the remnant oxide layer situated within metallic melts. The dependence of the reaction rates on the initial ZrO_2 layer thickness, which determines the final thickness of the α-Zr(O) layer, is not well expressed.

As a first attempt, especially for transient conditions, an averaged value of the reaction rates can be used neglecting the dependence on the initial oxide layer. A more sophisticated description is beyond the scope of this report, because the oxide layer dependence as well as the different temperature ranges have to be included (see Figure 13).

As can be seen from Figure 13 ,the dependence of the activation energy on the initial oxide layer thickness is within the accuracy of the measurements. So far it is not clear why the reaction rates on both sides of the Matano interface show slightly different change in the temperature dependence at app. 1480 K. One possible explanation is that the phase transition from monoclinic to tetragonal ZrO_2 allows a faster diffusion of the Fe and Ni ions through the oxide. The fast liquefaction is shifted to temperatures above 1573 K due to the limited velocity of the diffusing species and the larger oxygen concentration in the liquid and solid materials.

4.2.2.3. Inconel 718 / Zry

A comparison of the reaction rates of the as-received material interactions Inconel/Zry (s. Figure 8) with those obtained with pre-oxidized Zry (s. Figure 14) reveals an increasing temperature dependence with increasing initial oxide layer thickness beyond an initial oxide layer of 10 μm. Above 1523 K the difference levels out for all reaction rates until fast liquefaction occurs at around 1580 K. Generally, the database is limited and the accuracy of the measurements is not sufficient to clarify the reasons of the observed microscopic behavior completely.

If the spatial distribution of the oxygen is nearly uniform, for example if the sample is annealed in vacuum for long time, so that the initial ZrO_2 layer is completely reduced to α-Zr(O), then

nearly the same temperature dependence is obtained /21/. The diffusion coefficients of Fe and Ni in Zr, however, are approximately five times larger in β-Zr than in α-Zr at 1200 K (s. Table 13). The measured reaction rates differ by more than two orders of magnitude. One possible explanation may be the high oxygen content dissolved in the metal, hindering the interstitial diffusion mechanisms of the Fe and Ni by blocking interstitial sites. If the ratio of the reaction rates is applied to the diffusion coefficient of Fe or Ni in α-Zr(O), than a value in the range of the oxygen diffusion is achieved.

This finding is also supported by the change in the slope of the measured reaction rates at around 1480 K. This change, associated with the phase transformation, increases the oxygen diffusion coefficient in the ZrO_2. If the oxygen diffusion is the limiting process in the ZrO_2 as well than in the α-Zr(O) , than the oxygen mobility in the tetragonal oxide has to be the same or even higher as in the α-Zr(O) (s. Table 13). This hypothesis has to be supported be measurements of the oxygen concentration in the samples and the thickness of the remnant oxide layer. The deviations between the slopes discussed herein and those drawn in Figure 14 can be explained by the limited accuracy. As a first recommendation an extended rate equation is given which also considers the oxygen dependence of the experimental results.

$$k_p(\delta,T) = \delta_{Ox}^{A_1} * A_2 * \exp\left(-\frac{Q'}{RT}\right), \quad \text{with:} \quad Q' = A_3 * (1 - A_4 * \delta_{Ox}^2) * R. \tag{12}$$

with parameters A_1 ..A_4 defined from experimental results. The results are summarized together with those of the incubation times in Table 12. For calculations of transient integral experiments or even reactor transients, however, the correlations obtained here may be sufficient, since the boundary and contact conditions, the initial oxide layer thickness and its behavior during heat-up give rise to a much larger uncertainty.

4.3. MODELLING OF THE AG/ZRY AND (AG,IN,CD)/ZRY INTERACTIONS

From the present understanding an adequate description of low temperature material interactions during LWR SFD accidents has to include two major processes:

1. dissolution of the ZrO_2 layer by oxygen diffusion into the β-Zry, forming a growing layer of α-Zr(O), and
2. dissolution of the Zry by diffusion processes which are dependent on temperature and oxygen concentration in the β-Zry and α-Zr(O).

Since the basic processes are diffusion in the solid state and in the liquid layer formed due to the eutectic reaction, only the solution of the relevant diffusion equation(s) can lead to reliable results, especially when two liquid-solid interfaces are formed. If the diffusional mass transport in the liquid is larger than the convective one no ideal mixing can be assumed, so that a concen-

tration profile in the liquid has to be calculated, depending on the boundary concentrations and the thickness and geometry of the liquid layer.

Since the (Ag,In,Cd)/Zry system is quite complicated and the database, such as boundary concentrations and diffusion coefficients, is limited the Ag/Zr system will be discussed first. In this case the mass transport of the dissolved Zr into the liquid can be calculated from the interface movement measured in the experiments.

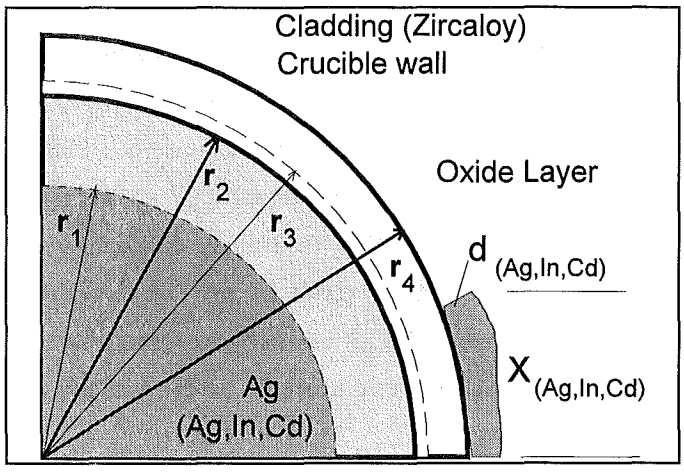

In the schematics on the left side the different dimensions are given:
r_1 denotes the inner radius of the liquid (= 0 for separate-effects test),
r_2 the interface to the Zircaloy cladding or crucible,
r_3 is the interface oxide / α-Zr(O),
r_4 is the outer diameter of cladding or crucible.

The phenomenological model is based on quasi stationary conditions, so that for a time step Δt the temperature does not change. Than the actual position of the interface ξ(t+Δt) can be calculated as:

$$\xi(t+\Delta t) = \left(\xi(t)^2 + k_p * \Delta t\right)^{0.5}, \quad \text{with} \quad k_p = A_{\exp} * \exp\left(-Q/RT\right), \tag{13}$$

with the boundary concentrations discussed in section 4.1.1. and 4.1.2. For the calculation of separate-effects tests and for reactor purposes, the following limitations have to be checked:

1. the average concentration of Zr in the liquid alloy c_{lim} = f(T), and
2. the amount of solid Zr consumed due to liquefaction : $r_{2,(t=0)} + \xi_{(t+\Delta t)} < r_4$.

For reactor purposes where the liquid alloy relocates down the cladding surfaces for a limited time, the mass and the average chemical composition of the liquid alloy has to be checked. In case of the control rod alloy, a modified quasi binary phase diagram (Ag, In)/Zr is required.

For item 1 a global mass balance is required to calculate the increasing Zr concentration in the liquid while the mass of the absorber alloy is assumed to be constant (separate-effect tests).

$$m_{Zr(t+\Delta t)} = m_{Zr(t)} * \Delta V_{(t)} * \rho_{Zr(T)} \qquad \text{with:} \qquad \Delta V_{(t)} = \left(r^2_{2(t-\Delta t)} - r^2_{2(t)}\right) * \Pi * h_l , \tag{14}$$

where r_2 is the interface ξ (see schematics above) and h_l is the axial length of the liquid-solid interface in the test capsule. The volume increase due to liquefaction and thermal expansion is

not yet considered. Then the average concentration of Zr in the liquid alloy, which is important to determine the solidus temperature for subsequent material relocations, can be calculated by:

$$\tilde{C}_{(t+\Delta t)} = \frac{m_{Zr}}{m_{Zr} + m_{Ag}}, \text{ in wt \%} \qquad \text{with : } m_{Ag\,(t+\Delta t)} = r_2^2 * \Pi * h_l, . \tag{15}$$

However, the concentration profile in the liquid layer is not determined since intermetallic compounds (AgZr, $AgZr_2$) may exist below 1426 K. For a precise determination of saturation effects the diffusion equation has to be solved and the solubility limits given by the relevant binary or pseudo-binary phase diagram have to be checked.

In case of thin initial oxide layers and under isothermal conditions the calculation of the Zry dissolution starts when the annealing time exceeds the calculated incubation time (s. Eq. 2). For transient conditions, however, the actual incubation time is calculated for each time step considering the actual cladding temperature and the actual oxide layer thickness. For integral tests the calculation of the incubation times is started at the time when the cladding temperature exceeds a critical temperature. This temperature is assumed to be the lowest eutectic temperature of the calculated interaction type, since significant interactions have to be expected only when a liquid phase has been formed as a result of the chemical interaction.

So the incubation time is not a fixed time period, since the temperature increase also enhances the oxygen diffusion coefficient, accelerating the dissolution of the oxide layer. If the time difference in Eq. (15) is less than zero, the calculation of eutectic interaction starts using the reaction rates measured for an initial oxide layer of 10 µm.

$$\Delta t_{(t+\Delta t)} = t_{system} - \left(t_{0,(T,\delta_{Ox})}^{(t+\Delta t)} + t_{contact} \right), \tag{16}$$

Using the experimental reaction rates from the (Ag,In,Cd)/Zry or Ag/Zry interaction the movement of the interface ξ can be calculated respectively by Eq. (12). The oxygen concentration is neglected.

In integral tests as well as in SFD accidents, the boundary conditions are not so well defined as in separate-effects test discussed here. Moreover, flowing control rod melts would complicate the interaction, but in this case saturation can be neglected, because during relocation always material of initial chemical composition will interact with the Zircaloy. After relocation some absorber alloy remains at the cladding surface, so that in this case the thickness is small compared with the cladding thickness. The relevant thickness of the remained absorber alloy attached to the cladding surface can be obtained by detailed post-test investigations of integral tests (e. E. CORA-7).

5. TRANSIENT BEHAVIOR

As already pointed out in section 2, the environmental conditions in a severe core damage accident of a LWR or in a simulation (integral in-pile or out-of-pile tests) are quite different from those of the separate-effects tests. Instead of isothermal and well-defined contact conditions between the materials, fast temperature increases (up to several tens of K/s) due to the exothermal zirconium/steam reaction and undefined contact pressures have to be considered in reality. Due to the strong temperature dependencies of the interactions discussed herein, the transient heat-up strongly influences the kinetic behavior of the interactions.

From integral tests, informations on intermediate states cannot be extracted easily from the post-test state of a degraded fuel rod bundle. To overcome this deficiency, results of calculations using integral codes have to be used. As already pointed out (s. section 2.2) in a fuel rod bundle, which is only a small scale simulation of a complete reactor core, various processes occur at the same time and may interact or influence each other. Generally, such interactions are very complicated and have to be investigated in detail. For the purposes of this paper, however, only processes which may initiate or trigger other processes will be discussed (process chaining) with respect to the global behavior of a bundle or a core.

5.1. SEQUENCE OF MATERIAL INTERACTIONS DURING HEAT-UP

As an attempt to demonstrate the influences between individual processes at different spatial positions Figure 3 was developed, based on the findings of integral test in the out-of-pile facility CORA, separate-effects tests and code calculations. The primary goal is to determine the influence of localized processes on the global course of a SFD accident. Moreover, capabilities to enhance reactor safety in the temperature range of "low-temperature" material interactions can be extracted. Figure 3 only represents the states of a horizontal cut through a fuel rod bundle or fuel rod element. No information about the variation of the states in vertical direction can be obtained, since the axial temperature gradient, which is influenced by heat transport mechanisms such as melt relocation, convection, and/or radiation, is not considered in this schematic. A separation of processes occurring at control rod assemblies and fuel rods is important to clarify that different separate processes take place at the same time with subsequent interactions.

From the various parameters, determining the course of a SFD accident after a reactor scram and core uncovery, two basic parameters, the pressure ratio, calculated from the internal rod pressure and the system pressure, and the time since core uncovery are selected to show their influence on the processes in the temperature range of "low-temperature" material interactions.

- The pressure ratio controls the mechanical cladding deformation, leading to ballooning ($\Delta p \gg 1$) or collapsing ($\Delta p \ll 1$) of the cladding. If the pressure difference is small ($\Delta p > 1$), the burst temperature is very high, so that a perforation due to eutectic reactions release the gaseous inventory (fill gas plus gaseous fission products) and small amounts of metallic melt (shown as double line in mech. behavior of Figure 3).
- Two heat sources determine the heat-up rate after core uncovery: primary, the decay heat of the fission products, which is only determined by the power history of the reactor and the time since scram, and secondary, the exothermal zirconium/water reaction, controlled by the oxygen supply and the initial oxide layer thickness.

Below 1200 K only mechanical deformation of the cladding due to the pressure difference is significant. An early solid state contact is achieved due to the high system pressure of the "high-pressure case", enhancing the fuel-clad interactions. In the "low-pressure case" plastic deformation called "ballooning" locally prevents this contact, but increase the cladding surface after clad rupture so the gaseous fission products are released and oxidation of the inner surface take place later on.

The temperature range between 1200 K and 1790 K is dominated by the fast heat-up rates above 1500 K due to the exothermal zirconium/steam reaction. Eutectic interactions at the control rods (SS / Zry) and at spacer grids (Inconel / Zry) locally liquefy cladding material with subsequent release of gaseous inventory and metallic melts, [(Ag,In,Cd) + (Fe, Ni, Zr)] mixtures.

In the low-pressure case the liquid control rod alloy is sprayed on the cladding surfaces of adjacent fuel rods. There, the melt relocates down, stopping the oxidation and starts to interact with the Zircaloy after dissolution of the oxide layer. All liquid absorber alloy above the location of the breach is released. If the liquid alloy contacts the cladding surface of adjacent fuel rods direct chemical interactions at the control rods initiate chemical processes at the fuel rods. Up to this time the chemical processes in the control rods and in fuel rods did not interact with each other due to the spatial separation.

In all the PWR CORA tests analyzed so far, the failure of control rods or fuel rod claddings due to eutectic interactions occurred below the melting point of SS or Inconel, respectively /3, 5/.

Between 1790 K and app. 2300 K, high-temperature cladding deformation ("flowering" /4/) occurs which may be initiated by a dissolution of the ZrO_2 layer due to relocated metallic melt (Fe, Ni, Zr, O) on the outer cladding surface, which prevents further oxidation. The melting of metallic β-Zry ($T_m \approx 2033$ K) intensifies the fuel-cladding interaction ("low-pressure case"). The oxygen solubility in the liquid β-Zry lead to a local thinning of the α-Zr(O) and the ZrO_2 layer so that breaching can occur at ≈ 2230 K. After the release of the liquid (Zr, U, O) mixture the subsequent oxidation of inner cladding surface can lead to a high-temperature cladding deformation

too. Both processes locally declad the fuel pellet stacks and prevent them from further fuel clad interaction /5/. Damage continues and changes from a primarily local to a global character. Control rod alloy relocates as rivulets forming blockages in the lower regions of the bundle or core. Non-coherent melt relocation dominates the damage propagation in vertical direction /5/.

Above 2300 K, the character of the melts is primarily ceramic, with large amounts of uranium. The higher solidification temperatures lead to early freezing. The heat-up rates are reduced due to the increasing oxide layers and the already high oxygen concentrations in the ceramic melts. Above app. 2700 K, material interactions do not play an important role since nearly all materials are liquid due to melting or eutectic interactions.

5.2. TIME SCALES DURING HEAT-UP

After core uncovery the energy released by the zirconium/steam interaction controls the heat-up rate and the maximum temperature. As was found in integral experiments, the time scales, especially for the temperature range of "low-temperature" material interactions are strongly influenced by the initial heat-up rate. Furthermore, the reaction kinetics are determined by the initial oxide layer thickness. Both factors determine a range in which the "low-temperature" material interactions become significant for the subsequent processes.

On the right side of Figure 3 the time scales for an upper and lower limit of the heat-up rate are given. Above app. 1.5 K/s the system only requires app. 200 s to reach 1790 K , the liquifaction temperatures of SS or Inconel alloys. This time interval is too short for a significant damage due to eutectic interactions.

Below app. 0.3 K/s the system stays more than 1600 s below 1473 K, sufficiently long to create thick oxide layers on the unprotected or unshielded cladding surfaces. These thick oxide layers also limit the subsequent heat-up rate beyond 1500 K from app. 12 K/s to less than 2 K/s. The whole time interval increases up to more than 2000 s, which is long enough to allow fuel rod damage due to eutectic interactions. But, if sufficient oxygen is supplied to the cladding, the increasing oxide layers inhibit these interactions below 1470 K. So only a 300 s long time interval separates eutectic interactions from melting of the initial materials.

At moderate heat-up rates 0.3 K/s < dT/dt < 1.5 K/s, cladding perforation and interactions between control rod alloys (Ag,In,Cd) and structure materials (SS, Inconel) take place long before melting of the original alloys. As can be seen from Figure 3 various reaction paths are possible depending on the boundary conditions (pressure ratio, temperature heat-up rate). Chemical reactions in the temperature region of "low-temperature" material interactions strongly influence the further reaction path.

6. SUMMARY AND CONCLUSION

The results of separate-effects tests on chemical interaction studies have been reviewed with respect to fuel element and core structure materials such as Zircaloy, stainless steel (AISI 304, 316), Inconel 718, control rod alloys (Ag,In,Cd) and B_4C in the temperature range between 1200 K and 1700 K ("low-temperature"). The results obtained at KfK are compared with those measured at JAERI and with additional data from the literature.

For each of the investigated material interaction couples, the experimental boundary conditions have been described, discussed and compared to check the possible experimental effects such as different sample geometries or mass ratios on the reaction kinetics. Also the various Arrhenius correlations derived from the measurements have been checked and compared.

For the interaction system (Ag,In,Cd) / Zry the different measured reaction rates fit very well with each other. The basic interaction process is the diffusion of Zr into the liquid Ag or (Ag,In,Cd) alloy. In case of the Ag/Zr system the diffusion coefficients could be estimated from the reaction rates and the binary phase diagram and the diffusion of that in the (Ag,In,Cd) alloy was estimated from the measured phase boundary concentrations. The estimated diffusion coefficients are one order of magnitude smaller than the self-diffusion coefficients in liquid Ag and two orders of magnitude larger than the diffusion of Ag in solid Zr. That means Zircaloy is liquefied by the absorber alloy.

The results of the investigations in the systems stainless steel / Zircaloy and Inconel / Zircaloy show some differences between KfK and JAERI results, which may be explained by the higher Zr mass inventory used at JAERI.

The kinetic results of the chemical interactions B_4C / Zircaloy indicate a similar behavior in the various tests. In case of B_4C / stainless steel the kinetic results of JAERI show a jump in the reaction rates at 1480 K probably due to formation of a liquid phase. This behavior was not observed in the KfK experiments.

The measured reaction rates in separate-effects tests performed with pre-oxidized Zircaloy (10 - 100 μm ZrO_2 layers) show a delay in the onset of the interactions . First a complete reduction of the ZrO_2 layer by diffusion of oxygen into the β-Zry forming an α-Zr(O) layer is required to initiate the chemical interactions. As soon as the oxygen concentration in the ZrO_2 is reduced to that in α-Zr(O) the chemical interaction starts. The observed reaction kinetics are reduced due to the increased oxygen concentration in the Zircaloy metal lattice. Below 45 μm ZrO_2 thickness the delay times can be explained by oxygen diffusion, above, the increased porosity of the oxide reduces the delay time.

7. ACKNOWLEDGEMENTS

The authors wish to thank Dr. H. Uetsuka, Dr. F. Nagase, and Dr. T. Otomo from JAERI for submitting the unpublished results of their measurements. We also express our thanks to Dr. M. Veshchunov, Nuclear Safety Institute of the Russian Academy of Science (Moscow) for his support concerning analytical considerations and the fruitful discussions during the preparation of this report, and Dr. T. Haste for his thorough and critical review of this paper.

This work was partially funded by the Commission of the European Communities under the Reinforced Concerted Action "Core Degradation", Contract Number FI3S-CT-0001.

8. REFERENCES

/1/ Hobbins R.R, Petti A.D., Osetek D.J., Hagrman D.L.: Review of Experimental Results on Light Water Reactor Core Melt Progression, NT Vol.95 (1991) 287-307

/2/ Hofmann P., Hagen S., Schanz G., Skokan A.: Chemical Interactions of Reactor Core Materials Up to very High Temperatures, KfK 4485 (1989), NT Vol. 87 (1988) 146-186.

/3/ Hering W.: Modellierung des Experimentes CORA und Interpretation von Versuchsergebnissen mit dem erweiterten Kernschmelzcode Code SCDAP/MOD1, IKE 2-100 (1993).

/4/ Minato K., Hering W.: Zircaloy Oxidation and Cladding Deformation in PWR-Specific CORA Experiments, KfK 4827 (1991).

/5/ Hering W., Minato K., Nagase F.: Global Analysis of Bundle Behavior in Pressurized Water Reactor specific CORA-Experiments, NT Vol.102 (1993) 100-115.

/6/ Hagen S., Hofmann P., Noack V., Schanz G., Schumacher G., Sepold L.: Results of SFD Experiment CORA-13 (OECD International Standard Problem 31), KfK 5054 (1993).

/7/ Burbach J.: Ergebnisse von REM Mikrobereichsanalysen des DWR Bündelabschmelzexperiments CORA-13, KfK 5162 (1993).

/8/ Kleykamp H., Pejsa, R.: Chemical and X-ray Diffraction Analysis on Selected Samples from the TMI-2 Reactor Core, KfK 4872 (1991).

/9/ Wang H., Lück R., Predel B., Thermodynamic Investigation on Liquid Iron-Nickel-Zirconium Alloys, JPE Vol. 14 No. 1 (1993) 48-53.

/10/ Massalski T.B., Binary Alloy Phase Diagrams, Vol. 1, 2, and 3, American Society for Metals, Materials Park, Ohio (1990).

/11/ Zhang, K., Zhao H., Zhou Y., An Investigation of the Ag-Zr Phase Diagram, JLCM 138 (1988)173-177.

/12/ Schanz G., Leistikow S., Adelhelm Ch., Zur konkurierenden Sauerstoff- und Wasserstoffaufnahme des Zircaloy-4 bei hohen Temperaturen, Gase in Metallen, Deutsche Gesellschaft für Metallkunde, ISBN-3-88355-086-8 (1984) 413-426

/13/ Kummerer K.: Werkstoffe der Kerntechnik, Teil III: Hüll und Strukturwerkstoffe, Verlag G. Braun, (1980) 63-90.

/14/ Hofmann, P., Markiewicz, M.: Chemical Behavior of (Ag,In,Cd) Absorber Rods in Severe LWR Accidents, KfK 4670 (1990).

/15/ Hofmann, P., Markiewicz, M.: Liquifaction of Solid Zircaloy-4 by molten (Ag,In,Cd) Absorber Alloy, to be published in JNM (1994) .

/16/ Nagase, F.: private communication, 1988.

/17/ Nagase F., Otomo T., Uetsuka H., Furuta T.: Interaction between Silver-Indium-Cadmium Control rod Alloy and Zircaloy-4 at High Temperatures, JAERI-M-92-001 (1992).

/18/ Nagase F., Otomo T., Uetsuka H., Furuta T.: Interaction between Silver and Zircaloy-4 at High Temperatures, JAERI-M-92-179 (1992).

/19/ Patil R.V., Self-diffusion in Zr-Ag alloys, JNM 187 (1992) 197-203.

/20/ Petti, D.A.: Silver-Indium-Cadmium Control Rod Behavior and Aerosol Formation in Severe Reactor Accidents, NUREG/CR-4876 (EG&G-2501), (1987).

/21/ Hofmann, P., Markiewicz, M.: Interactions between As-received and Pre-oxidized Zircaloy-4 and Stainless Steel at high Temperatures, KfK-5106, to be published in 1994.

/22/ Nagase F., Otomo T., Uetsuka H., Furuta T.: Interaction between Stainless Steel and Zircaloy-4 at high Temperatures, JAERI-M-04-256 (1993).

/23/ Shaaban H.I., Hammad F.H., Baron I.L., Investigation of Diffusion-Bonding between Zircaloy-4 and 304 Stainless Steel, JNM 71 (1978) 277-285.

/24/ Warren, M.R., Rørbo, K., Adolph, E., Incompatibility between Zry-2 and Inconel X-750 during Temperature Transients, JNM 58 (1975) 185-188.

/25/ Garcia, E.A., Hofmann, P., Denis A.: Analysis and Modelling of the Chemical Interactions Between Inconel Grid Spacers and Zircaloy Cladding of LWR Fuel Rods; Formation of Liquid Phases due to Chemical Interactions, KfK 4921 (1992).

/26/ Hofmann, P., Markiewicz, M.: Chemical Interactions between As-received and Pre-oxidized Zircaloy-4 and Inconel 718 at High Temperatures, KfK-4729, to be published in 1994.

/27/ Veshchunov M., private communication, Sept. 1993 and Febr. 1994.

/28/ Nagase F., Otomo T., Uetsuka H., Furuta T.: Interaction between Zircaloy Tube and Inconel Spacer Grids at High Temperatures, JAERI-M-90-165 (1993).

/29/ Hammad F.H., Shaaban H.I., Interdiffusion of Zircaloy-4 and Nickel, JNM 80 (1979) 152-158.

/30/ Nagase F., private communication, Oct. 1993.

/31/ Hofmann, P., Markiewicz, M.: Reaction Behavior of B_4C Absorber Material with Stainless Steel and Zircaloy in Severe LWR Accidents, KfK-4598 (1989) , NT Vol. 90 (1990) 226-244.

/32/ Nagase F., Otomo T., Uetsuka H., Furuta T.: Transactions Volume 69 (1993) 309-311.

/33/ Veshchunov M., Hofmann, P.: Modelling of the B_4C Interaction with Zircaloy at High Temperatures, to be published in JNM, 1994.

/34/ Turkdogan E.T., Physical Chemistry of high Temperature Technology, Academic Press, London, ISBN 0-12-6704650-X (1980) 115.

/35/ Landold, Börnstein, Diffusion in Solids, Springer Verlag, Group III-26.

/36/ Tendler R., Abriata J.P., Atomic Size and Fast Diffusion of Metallic Impurities in Zirconium, JNM 150 (1987) 251-258.

/37/ Vieregge, K., Herzig, Ch., Tracer Diffusion of Silver in α-Zirconium Single- and Polycrystals, JNM 165 (1989) 65-73.

/38/ Nakajima, H., Hoods, G.M., Schultz, R.J., Diffusion of ^{59}Fe in single Crystal α-Zr, Phil.Mag. B Vol. 58 (1988) No. 3, 319-337.

/39/ Dayananda, M.A., Behnke, D.A., Effective Interdiffusion Coefficients and Penetration Paths, Script Metall. Vol.25 (1991) 2187.

/40/ Bhanumurthy K., Kall G.B., Khera S.K.: Reaction Diffusion in the Zirconium-Iron System, JNM 185 (1990) 208-213.

/41/ Pelton, A.D., Leibowitz, L., Blomquist, R.A., Thermodynamic Analysis of Phase Equilibria in the Iron-Zirconium System, JNM 201 (1993) 218-224.

/42/ Bhanumurthy K., Kall G.B., Khera S.K., Asundi M.K.: Solid-state Diffusion Reaction and Formation of Intermetallic Compounds in the Nickel-Zirconium System, Metall.Trans. 21A (1990) 2897-2903.

/43/ Aldebert P., Traverse J-P., Structure and Ionic Mobility of Zirconia at High Temperature, JAC 68,1 34-40 1985.

/44/ Pêcheur D., Lefebvre F., Motta A.T., Lemaignan C., Wadier J.F., Precipitate Evolution in the Zircaloy-4 oxide layer, JNM 189 (1992) 318-332.

/45/ Sofer, G.A., Busselmann, Federico, L.J., Weiterentwicklung von DWR- und SWR-Brennelementen, ATW, August-September (1988) 449-452.

Abbreviations:

ATW	Atomwirtschaft
IKE:	Institut für Kernenergetik und Energiesysteme, Universität Stuttgart
JAC:	Journal of the American Ceramic Society,
JAERI:	Japan Atomic Energy Research Institut
JLCM	Journal of the Less Common Metals
JMR:	Journal of Materials Research
JNM:	Journal of Nuclear Materials
JPE	Journal of Phase Equilibria, Section I.: Basic and Applied Research
KfK:	Kernforschungszentrum Karlsruhe, Germany
NT:	Nuclear Technology,

9. APPENDIX

9.1. LIST OF TABLES

9.2. LIST OF FIGURES

Figure 11: Isothermal section of the ternary phase diagram of Fe-Ni-Zr /8/ and the relevant binary phase diagrams Fe-Zr and Ni-Zr above 1200 K. The corresponding tie lines are given as thin dashed lines between β-Zr and stainless steel (open circle) and Inconel (solid circle)

Figure 12: Measured incubation times for various initial oxide layer thicknesses for the couples: (Ag,In,Cd) / Zry, SS 316 / Zry, and Inconel / Zry.

Figure 13: Measured reaction rates $x^2/(t\text{-}to)$ for various initial oxide layer thicknesses for the chemical interaction couple: stainless steel / Zry.

Figure 14: Measured reaction rates $x^2/(t\text{-}to)$ for various initial oxide layer thicknesses for the chemical interaction couple: Inconel / Zry.

Table 1: List of chemical interactions found in the examinations of the TMI-2 core bore samples analyzed at KfK /8/.

Type A melting reactions	
<absorber> = {Ag,In,Cd}	T_{sol} = 760 °C
<Inconel,steel> + <Zry> = {Fe,Cr,Ni,Zr,Sn}	$T_{eut} \cong$ 1200 °C*
<steel> + {absorber} = {Fe,Cr,Ni} + {Ag,In,Cd}	T_{mon} = 1435 °C
<steel> + <Mo,Tc,Ru,Rh,Pd> = {Fe,Ru,...}	T_{sol} = 1433 °C
Exchange reaction in the liquid	
{Fe,Cr,Ni,Zr,Sn} + {Ag,In,Cd} = {Fe,Cr,Ni,Zr} + {Ag,In,Ni,Sn} + (Cd)	T > 1435 °C
Side reaction during cooling	
{Ag,In,Ni,Sn} = {Ag,In,Sn} + <Ni_3Sn_2>	T_m = 1264 °C
Type B melting reactions	
{Fe,Cr,Ni,Zr} + <UO_2> = {Fe,Cr,Ni,Zr,U,O}	T ≥ 1300 °C
Main metallic reactions during cooling (St = Fe,Cr,Ni)	
{Fe,Cr,Ni,Zr,U,O} = <U(Zr)O_2> + {St,Zr; U,O depleted}	T < 2200 °C
{St,Zr; U,O depleted} = {St,Zr,U,O} + <$ZrSt_2$>	T_m = 1675 °C
{St,Zr,U,O} = <U(Zr)O_2> + <$StZr_2O_x$>	T ≥ 1600 °C
Type C melting reactions	
<UO_2> + <ZrO_2> → <(U,Zr)O_2> = {(U,Zr)O_2}	T_m = 2550 °C
<Al_2O_3> + <Zr> = {Zr,Al,O}	T_{eut} ≥ 1350 °C
<$FeAl_2O_4$> = {$FeAl_2O_4$}	T_m = 1770 °C
<$FeCr_2O_4$> = {$FeCr_2O_4$}	T_m = 2150 °C
Main ceramic reactions during cooling	
{(U,Zr)O_2} = <(U,Zr)O_2>	T_{sol} ≥ 2550 °C
<(U,Zr)O_2> = <U(Zr)O_2> + <Zr(U)O_2>	T ≥ 1600 °C
{U,Zr,Al,Fe,Cr,O} = <(U,Zr)O_2> + <$Fe(Al,Cr,Zr)_2O_4$>	T_{eut} = 1500 °C
Oxidation at higher oxygen potentials	
<$StZr_2O_x$> + O_2 = <St_3Zr_3O>	

* a further invariant point in the pseudo-ternary exists at 930 °C which may give rise to local liquefaction; it is masked by fast $Zr(Fe,Cr,Ni)_2$ Laves phase formation.

Table 2: Measured reaction rates (m^2/s) for the diffusion couples: Ag / Zry and (Ag,In,Cd) / Zry as-received and for (Ag,In,Cd) / Zry with an initial oxide layer of 10 μm.

Ag / Zry-4			**JAERI**			**KfK**	
			Zircaloy - Interface				
T / °C	T /K	1.E4/T	min	Correl.	max.		
1000	1273	7.9	2.6E-12	7.7E-12	6.0E-12		
1050	1323	7.6	2.5E-11	5.8E-11	8.3E-11	no experiments	
1100	1373	7.3	2.1E-10	3.8E-10	3.1E-14	performed	
1150	1423	7.0	1.9E-09	2.1E-09	3.1E-09		
1200	1473	6.8	3.6E-08	1.1E-08	1.3E-08		

(Ag,In,Cd) / Zry-4			**JAERI**			**KfK**		
			Zircaloy - Interface			Zircaloy - Interface		Zry - Interface
T / °C	T /K	1.E4/T	average	Correl.	max.	max.	Correl.	**Correl. (1993)**
1000	1273	7.9	1.2E-10	1.9E-10	1.4E-10	2.6E-10	2.5E-10	
1050	1323	7.6	6.2E-10	6.2E-10	6.7E-10		8.6E-10	
1100	1373	7.3	3.1E-09	1.9E-09	3.3E-09	2.6E-09	2.7E-09	6.711E-10
1150	1423	7.0		5.3E-09		7.4E-09	7.8E-09	3.093E-09
1200	1473	6.8	8.3E-09	1.4E-08	1.0E-08	2.2E-08	2.1E-08	1.285E-08

(Ag,In,Cd) / Zry-4			**KfK: 10 μm ZrO_2**				**Incubation time**
			(Ag,In,Cd) - Interface			Zircaloy - Interface	
T / °C	T /K	1.E4/T	min	Correlat.	max.	max. Correlat.	t_0 /s
1000	1273	7.9				7.5E-11 7.1E-11	283
1050	1323	7.6	**liquid at temperature**			1.8E-10	--
1100	1373	7.3				4.1E-10 4.3E-10	65
1150	1423	7.0				8.6E-10 9.8E-10	
1200	1473	6.8				2.4E-09 2.1E-09	

Table 3: Measured reaction rates (m^2/s) of the interaction couples: stainless steel / Zircaloy, with as-received and pre-oxidized Zircaloy.

Zry / SS 316			JAERI						KfK					
			Zry - Interface			SS 304 -Interface				Zry - Interface		SS 316 -Interface		
T / °C	T /K	1.E4/T	min	Correl.	max	min	Correl.	max		max	Correl.	max	Correl	
1000	1273	7,9	9,84E-12	1,74E-11	1,02E-11	3,26E-13	1,60E-12	1,06E-12		9,48E-12	1,17E-11	5,74E-14	5,93E-14	
1050	1323	7,6	1,08E-10	9,72E-11	1,24E-10	3,69E-12	7,56E-12	6,94E-12			1,16E-10		6,93E-13	
1100	1373	7,3	4,98E-10	4,79E-10	7,46E-10	1,36E-11	3,20E-11	5,90E-11		1,44E-09	9,74E-10	8,72E-12	6,77E-12	
1150	1423	7,0	2,18E-09	2,11E-09	3,43E-09	7,50E-11	1,22E-10	1,60E-10		7,69E-09	7,04E-09	3,81E-11	5,64E-11	
1200	1473	6,8	4,32E-09	8,40E-09	6,70E-09	3,07E-10	4,26E-10	4,99E-10		3,33E-08	4,45E-08	4,79E-10	4,07E-10	
1250	1523	6,6	4,64E-09	3,06E-08	1,56E-08	3,85E-10	1,37E-09	7,82E-10						
1300	1573	6,4	5,18E-08	1,02E-07	1,32E-07									
	10 µ	ZrO2	Zry - Interface		Incubation time	SS 304 -Interface				Zry - Interface		Incubation time	SS 316 -Interfac		Incubation time
T / °C	T /K	1.E4/T	measured	Correl.	t0	min	Correl.	max		max	Correl.	t0 /s	max	Correl	t0 /s
1000	1273	7,9								-	-		-	-	
1100	1373	7,3			no experimental data available					1,90E-10	2,09E-10	426	9,70E-12	9,77E-12	371
1200	1473	6,8	3,53E-10		172					6,70E-10	1,33E-09	239	4,30E-11	4,34E-11	176
1300	1573	6,4	1,06E-10		32					1,20E-09	6,69E-09	83	2,10E-10	1,60E-10	56
	20 µ	ZrO2	Zry - Interface		Incubation time	SS 304 -Interface				Zry - Interface		Incubation time	SS 316 -Interfac		Incubation time
T / °C	T /K	1.E4/T	measured	Correl.	t0	min	Correl.	max		max	Correl.	t0 /s	max	Correl	t0 /s
1050	1323	7,6								1,67E-10	1,47E-10	7450	7,64E-12	7,58E-12	9770
1100	1373	7,3	no experimental data available			no experimental data available				2,50E-10	3,08E-10	3170	1,66E-11	1,69E-11	2870
1200	1473	6,8								1,25E-09	1,20E-09	800	7,16E-11	9,21E-11	710
1250	1523	6,6								3,95E-09	4,38E-09	250	7,43E-10	4,51E-10	310
1300	1573	6,4								1,54E-08	1,47E-08	205	1,53E-09	1,99E-09	170
	50 µ	ZrO2	Zry - Interface		Incubation time	SS 304 -Interface				Zry - Interface		Incubation time	SS 316 -Interfac		Incubation time
T / °C	T /K	1.E4/T	min	Correl.	t0	min	Correl.	max		max	Correl.	t0 /s	max	Correl	t0 /s
1100	1373	7,3								1,17E-10	8,21E-11	34060	8,03E-12	8,09E-12	35950
1200	1473	6,8				no experimental data available				9,47E-10	7,36E-10	4750	4,48E-11	4,90E-11	5470
1250	1523	6,6								1,78E-09	1,98E-09	1660	5,29E-10	4,51E-10	1890
1300	1573	6,4			300					4,67E-09	5,00E-09	640	3,29E-09	3,60E-09	610

Table 4: Measured reaction rates (m^2/s) of the interaction couples: Inconel 718 / Zircaloy, with as-received and pre-oxidized Zircaloy.

Zry / Inconel			JAERI						KfK					
			Zry - Interface			Inconel - Interface			Zry - Interface			Inconel - Interface		
T / °C	T /K	1.E4/	min	Correl.	max	min	Correl.	max	max	Correl.		max	Correl.	
1000	1273	7,9	4,19E-10	7,98E-10	7,85E-10	2,81E-11	4,01E-11	4,38E-11	2,17E-10	2,01E-10		3,25E-11	2,28E-11	
1050	1323	7,6	1,31E-09	2,03E-09	2,16E-09	4,91E-11	7,63E-11	6,59E-11		4,95E-10			6,53E-11	
1100	1373	7,3	3,17E-09	4,81E-09	4,25E-09	7,49E-11	1,39E-10	1,52E-10	9,40E-10	1,14E-09		7,74E-11	1,73E-10	
1150	1423	7,0	4,95E-09	1,07E-08	1,13E-08					2,48E-09			4,30E-10	
1170	1443	6,9		1,46E-08						3,33E-09			6,07E-10	
1170	1443	6,9		7,57E-08										
1200	1473	6,8	7,35E-08	1,15E-07	1,11E-07				5,66E-09	5,10E-09		1,55E-09	1,00E-09	
1250	1523	6,6	6,05E-08	2,22E-07	2,15E-07									
	20 µm	ZrO2	Zry - Interface			Inconel - Interface			Zry - Interface		Incuba-tion time	Inconel - Interface		Incuba-tion time
T / °C	T /K	1.E4/T	min	Correl.	max	min	Correl.	max	max	Correl.	to /s	max	Correl.	to /s
1100	1373	7,3							9,76E-10	8,85E-10	7175	6,79E-11	8,62E-11	6912
1150	1423	7,0								1,89E-09			4,11E-10	
1200	1473	6,8	no experimental data available			no experimental data available			3,18E-09	3,83E-09	314	2,95E-09	1,76E-09	339
1250	1523	6,6								7,41E-09			6,86E-09	
1300	1573	6,4							1,51E-08	1,38E-08	24	1,80E-08	2,45E-08	20
	45 µm	ZrO2	Zry - Interface			Inconel - Interface			Zry - Interface		Incuba-tion time	Inconel - Interface		Incuba-tion time
T / °C	T /K	1.E4/T	min	Correl.	max	min	Correl.	max	max	Correl.	to /s	max	Correl.	to /s
1100	1373	7,3							1,55E-10	1,34E-10	12900	1,12E-11	1,38E-11	9741
1150	1423	7,0								4,74E-10			1,19E-10	
1200	1473	6,8	no experimental data available			no experimental data available			1,14E-09	1,54E-09	276	1,42E-09	8,83E-10	340
1250	1523	6,6								4,61E-09			5,75E-09	
1300	1573	6,4							1,48E-08	1,29E-08	68	2,49E-08	3,32E-08	40

Table 5: Measured reaction rates (m^2/s) of the chemical interaction couples: B_4C / Zry and B_4C / SS, B_4C used in form of powder (KfK, JAERI) and pellets (JAERI).

B_4C/Zry								
Powder			JAERI			KfK		
T / °C	T /K	1.E4/T	Zry	Correl.	Correl/new	Zry	Correl. 1	Correl. 2
800	1073	9,3			*KfK 1993*	1,11E-15	4,44E-16	
900	1173	8,5	1,10E-15	6,18E-16	5,88E-16	6,61E-16	1,43E-15	
1000	1273	7,9	1,53E-15	2,60E-15	2,33E-15	1,80E-15	3,85E-15	
1100	1373	7,3	8,20E-15	8,87E-15	7,54E-15	1,01E-14	8,96E-15	
1200	1473	6,8	3,50E-15	2,56E-14	2,08E-14	1,96E-14	1,86E-14	
1300	1573	6,4	2,45E-14	6,46E-14	5,05E-14	4,89E-14	3,51E-14	
1400	1673	6,0	1,54E-13	1,46E-13	1,10E-13	6,83E-14	6,15E-14	
1450	1723	5,8	2,38E-13	2,12E-13	1,58E-13		7,94E-14	
1500	1773	5,6	3,41E-13	3,01E-13	2,20E-13	3,35E-13		3,36E-13
1550	1823	5,5	6,20E-13	4,19E-13	3,03E-13			4,88E-12
1600	1873	5,3	5,18E-11	3,66E-11		6,13E-11		6,15E-11
1650	1923	5,2	5,18E-11	6,46E-10				
1680	1953	5,1	6,20E-09	3,37E-09				

B_4C/Stainless steel								
Powder			JAERI			KfK		
T / °C	T /K	1.E4/T	SS 304	Correl. 1	Correl. 2	SS 316	Correl. 1	
800	1073	9,3	4,87E-15	5,09E-15		3,65E-16	3,48E-16	
900	1173	8,5	4,77E-14	7,61E-14		1,25E-14	1,29E-14	
1000	1273	7,9	2,14E-12	7,43E-13		2,48E-13	2,71E-13	
1100	1373	7,3	3,79E-12	5,21E-12		3,67E-12	3,65E-12	
1200	1473	6,8	2,32E-11	2,80E-11		3,62E-11	3,46E-11	
1250	1523	6,6	7,92E-09		1,10E-08			
1300	1573	6,4	5,77E-08		2,90E-08			
1350	1623	6,2	5,11E-08		7,23E-08			

B_4C/Stainless steel								
Pellets			JAERI			KfK		
T / °C	T /K	1.E4/T	SS 304	Correl. 1	Correl. 2	SS 316	Correl. 1	Correl. 2
800	1073	9,3	1,13E-14	1,01E-14				
900	1173	8,5	6,28E-14	1,10E-13				
1000	1273	7,9	1,96E-12	8,23E-13				
1100	1373	7,3	4,24E-12	4,60E-12		no experiments performed		
1200	1473	6,8	1,69E-11	2,03E-11				
1225	1498	6,7	1,00E-09		1,24E-09			
1250	1523	6,6	2,88E-09		2,53E-09			
1300	1573	6,4	1,16E-08		9,92E-09			
1350	1623	6,2	3,04E-08		3,57E-08			

Table 6: Experimental correlations of all investigated interactions with as-received Zircaloy.

		KfK				JAERI			
		Interface I		Interface II		Interface I		Interface II	
Couple	Temperature range /K	A m²/s	Q kJ/mol	A m²/s	Q kJ/mol	A m²/s	Q kJ/mol	A m²/s	Q kJ/mol
(Ag,In,Cd) / Zry	< 1473	liquid		3.55E4	344.87	liquid		1.23E4	336.8
Ag / Zry	<1473 *(<1423)* *(>1423)*	no experiments performed				liquid		3.49E12 *3.99E13* *5.18E9*	580.8 *603.6* *496.5*
SS / Zry	1273 - 1523	1.19E-6	435.6	1.02 E -9 (1.49E9*)	481.8 (571.6*)	1.08E15	688.8	2.78E15	642.8
Inconel / Zry	1273 - 1423,1473 - 1523	2.884E1	294.9	4.435	252.09	1.02E-3	180.5	40.8 59.7	261.0 245.8
B_4C / Zry	1073 -1773 1173 -1823 1823 -1953	no layer found		4.15E10 ***2.38E-8*** 7.94E37	122.6 ***170.8*** 1438.3	no layer found		5.38E-08 3.37E37	178.3 1720
B_4C /SS316 (powder)	1073 - 1473, 1498 - 1623	no layer found		876	378.0	no layer found		0.304 2.22E5	283.0 388.0
B_4C /SS 304 (pellets)	1073- - 1473, 1498 - 1623	no experiments performed				no layer found		1.49E-2 1.15E10	250.0 544.0

Table 6 contains the values for: $\mathbf{K_p = A \cdot exp\ (-Q/\ RT)}$, R= 8.314 kJ/mol K.
The correlation coefficients in Table 6 are calculated from the maximum layer thicknesses, the growth rates are defined as : $\mathbf{K_p} = \delta^2/_t$

Interface I : movement of the interface: diffusion zone - first material,
Interface II : movement of the interface: diffusion zone - second material:

(*) Results from shrinking measurements at KFKI, Budapest.

Table 7: Experimental correlations of all investigated interactions with pre-oxidized Zircaloy.

			KfK			
			Interface I		Interface II	
Interaction Couple	**Tempera-ture range /K**	**Initial Oxide Layer**	**A** m^2/s	**Q** kJ/mol	**A** m^2/s	**Q** kJ/mol
(Ag,In,Cd) / Zry	< 1473	10 µm	liquid		4.67	263.7
SS 316 / Zry	1323 -1573 1323 - 1473 --- 1473 - 1573	10 µm 20 µm 50 µm --- 20 µm 50 µm	0.034 0.028 0.815 --- 9.36E10 1.107E19	250.8 242.4 289.2 --- 592.4 827.8	1.43E2 0.103 8.93E3 --- 1.58E8 8.93E3	311.1 224.1 368.9 --- 482.8 368.9
(*)						
SS 316 / α-Zr(O)	1473 and 1573	α-Zr(O)	7.588E26	1101.6	5.408	282.1
Inconel / Zry	1373-1573	20 µm 45 µm	1.73E9 5.4E15	507.4 699.0	2.095 5.44E5	246.4 410.3

The correlation coefficients in Table 7 are calculated from the maximum layer thicknesses, the measured reaction rates are defined as :

$K_{p(ox)} = \delta^2/(t - t_0)$. $K_{p(ox)} = A * \exp(-Q/RT)$,

R = 8.314 kJ/mol K,

δ = position of interface at annealing time $t_m = t - t_0$.

The corresponding t_0 values are listed in Table 8.

(*) Results from JAERI not sufficient to calculate temperature dependencies

Table 8: Comparison of incubation times due to thin initial oxide layers on the Zircaloy surface for the interaction couples: SS 316 / Zry, Inconel 718 / Zry, and (Ag, In, Cd) / Zry

A: Stainless steel (AISI 316) / Zircaloy-4					
T / °C	*T /K*	*1.E4/T*	*10 µm*	*20 µm*	*50 µm*
1050	1323	7.558		8.6E+03	
1100	1373	7.283	4.0E+02	3.0E+03	3.5E+04
1150	1423	7.027	2.1E+02	1.6E+03	1.7E+04
1200	1473	6.788	7.0E+01	7.6E+02	5.1E+03
1250	1523	6.566	3.1E+01	2.8E+02	1.8E+03
1300	1573	6.357	1.4E+01	1.9E+02	6.3E+02

B: Inconel 718 / Zircaloy-4						
T / °C	*T /K*	*1.E4/T*	*10 µm*	*20 µm*	*45 µm*	*100 µm*
1100	1373	7.283	4.0E+02	7.0E+03	1.1E+04	
1150	1423	7.027	2.2E+02			
1200	1473	6.788	8.1E+01	3.3E+02	3.1E+02	8.5E+02
1300	1573	6.357		2.2E+01	5.4E+01	2.1E+02
1400	1673	5.977				3.1E+01

C: (Ag, In, Cd) / Zircaloy-4			
T / °C	*T /K*	*1.E4/T*	*10µm*
1000	1273	7.85	2.8E+02
1100	1373	7.28	6.6E+01
1150	1423	7.03	1.0E+01

Table 9: Diffusion coefficient of Zr in liquid Ag calculated from the measured Ag / Zr reaction rates and from boundary concentrations depicted from the binary phase diagram

Boundary Concentrations			Concentration gradients		Growth rate	Diffusion-coefficient	Correlation D_{eff} (T).	Deviation
Minimum Values					R = 8.314 J / mol K			
T /K	c_ξ^+ (Ag)	c_ξ^- (Ag)	Δc^I (Zr)	Δc_ξ (Zr)	$kp_{(mess)}$	D_{eff}	D_{eff} (T)	Δ D
1273	0.963	0.108	0.037	0.855	2.55E-12	*3.4E-10*	3.06E-11	91%
1323	0.80	0.13	0.2	0.67	2.48E-11	*6.96E-11*	7.85E-11	-13%
1373	0.73	0.17	0.267	0.567	2.14E-10	*2.41E-10*	1.88E-10	22%
1423	0.58	0.20	0.425	0.375	1.91E-09	*3.72E-10*	4.23E-10	-14%
1473	0.23	0.18	0.767	0.058	6.20E-09	*8.86E-12*	9.03E-10	-10084%
			Pre-exponential factor: D_0=				**2.038**	Correl.-
			Activation energy: Q =				**263762**	*coef.=0.969*
Average Values:								
T /K	c_ξ^+ (Ag)	c_ξ^- (Ag)	Δc^I (Zr)	Δc_ξ (Zr)	$kp_{(mess)}$	D_{eff}	D_{eff} (T)	Δ D
1273	0.963	0.108	0.037	0.855	4.21E-12	*5.62E-10*	7.01E-11	88%
1323	0.80	0.13	0.2	0.67	5.08E-11	*1.43E-10*	1.45E-10	-1%
1373	0.73	0.17	0.267	0.567	2.56E-10	*2.89E-10*	2.83E-10	2%
1423	0.58	0.20	0.425	0.375	2.68E-09	*5.22E-10*	5.28E-10	-1%
1473	0.23	0.18	0.767	0.058	9.83E-08	*1.41E-10*	9.45E-10	-573%
			Pre-exponential factor: D_0=				**0.015**	Correl.-
			Activation energy: Q =				**202795**	*coef.=0.999*
Maximum Values:								
T /K	c_ξ^+ (Ag)	c_ξ^- (Ag)	Δc^I (Zr)	Δc_ξ (Zr)	$kp_{(mess)}$	D_{eff}	D_{eff} (T)	Δ D
1273	0.963	0.108	0.037	0.855	6.03E-12	*8.05E-10*	1.32E-10	84%
1323	0.80	0.13	0.2	0.67	8.25E-11	*2.31E-10*	2.25E-10	3%
1373	0.73	0.17	0.267	0.567	3.10E-10	*3.49E-10*	3.68E-10	-5%
1423	0.58	0.20	0.425	0.375	3.08E-09	*5.99E-10*	5.82E-10	3%
1473	0.23	0.18	0.767	0.058	1.04E-07	*1.49E-10*	8.91E-10	-499%
			Pre-exponential factor: D_0=				**1.69E-04**	Correl.-
			Activation energy: Q =				**148829**	coef.=0.995

ΔD = deviation between correlation D_{eff} (T) and calculated diffusion coefficients D_{eff}
c_ξ^+ , c_ξ^- (Ag) = boundary concentrations of Ag from binary Ag-Zr phase diagram [11].

Table 10: Concentrations extracted from SEM-WDX measurements of the chemical interaction (Ag,In,Cd)/Zr between 1273 K and 1423 K **(A)**, at the boundary adjacent to the interface **(B)**, and estimated concentrations at different distances from the interface **(C)**.

A Sample	T /K	t /s	Phase type	c_{Zr} at%	c_{Ag} at%	c_{In} at%	c_{Cd} at%
164AB	*1273*	*300*	*black*	70	6	23	1
			light-gray	50	45	2	0
			dark-gray	57	9	33	1
166AB	*1273*	*1800*	*black*	57	9	33	1
			light-gray	--	82	4	14
			dark-gray	50	47	2	1
169AB	*1373*	*600*	*black*	51	47	1	1
			light-gray	---	67	32	1
			dark-gray	67	8	22	3
174AB	*1423*	*120*	*black*	54	12	32	2
			light-gray	--	76	3	21
			dark-gray	50	46	1	0.2

B Sample	T /K	t /s	Position	c_{Zr} at%	c_{Ag} at%	c_{In} at%	c_{Cd} at%
164AB	*1273*	*300*	*$x \approx 10$ µm*	52	43	5	0
166AB	*1273*	*1800*	*$x \approx 50$ µm*	55	37	6	16
169AB	*1373*	*600*	*$x \approx 10$ µm*	73	18	3	4
174AB	*1423*	*120*	*$x \approx 10$ µm*	--	--	--	--

C Sample	T /K	t /s	Position	c_{Zr} at%	c_{Ag} at%	c_{In} at%	c_{Cd} at%
164AB	*1273*	*300*	*$x \approx 180$ µm*	53	30	17	--
166AB	*1273*	*1800*	*$x \approx 185$ µm*	20	72	8	--
169AB	*1373*	*600*	*$x \approx 200$ µm*	62	31	7	--
174AB	*1423*	*120*	*$x \approx 410$ µm*	14	62	24	--

Table 11: Diffusion coefficients estimated from extracted SEM-WDX measurements of the chemical interaction (Ag,In,Cd)/Zry between 1273 K and 1373 K.

Diffusion coefficients of Zr in (Ag,In,Cd)/Zry						
Temperature	**Concen-tration**	**Concen-tration**	**Concen-tration**	**Difference at ξ**	**K_p (mess)**	**D_{eff} (Zr)**
T / K	c^+_ξ (Zr)	c^-_ξ (Ag)	c^-_ξ (Zr)	$\Delta c \xi$	**m²/s**	**m²/s**
1273	0.52	0.108	0.892	0.372	2.50E-10	***1.09E-11***
	0.55			0.342		***9.19E-12***
1373	0.73	0.17	0.834	0.104	2.70E-09	***1.05E-11***

Table 12: Results of a non-linear fit to the incubation times for (Ag, In, Cd) / Zry, SS 316 / Zry, and Inconel 718 / Zry

Reaction Couple	Temperature range /K	Oxide layer thickness range /μm	Parameter A0	Parameter A1	Parameter A2
Fit-Equation (13)			**Exponential (2 + Param 0)**	**Pre-exponen-tial factor s**	**"Activation energy" kJ / mol K**
(Ag,In,Cd) / Zry	1273 -1473	10 (< 20)	+ 0.110	0.352	333.05
SS 316 / Zry	1273 -1573	< 50	+ 0.475	$2.87 * 10^{4}$	280.36
Inconel 718 / Zry	1273 -1573	< 45	- 0.457	$6.49 * 10^{-9}$	502.94
Fit-Equation (14)			**'Fictive rem-nant' oxide layer /μm**	**Pre-exponen-tial factor s**	**"Activation energy" kJ / mol K**
(Ag,In,Cd) / Zry	1273 -1473	10 (< 20)	+ 12.52	13.59	308.36
SS 316 / Zry	1273 -1573	< 50	+ 12.61	1747.35	276.62
Inconel 718 / Zry	1273 - 1573	< 45	+ 13.07	$2.56 * 10^{-5}$	495.2

with: $$t_0(\delta_{Ox}, T) = A^{(1)} * \delta_{Ox}^{(2-A^{(0)})} * \exp(Q/RT) \quad (13)$$

or $$t'_0(\delta_{Ox}, T) = A^{(1)} * (\delta_{Ox} - \delta_{rem})^2 * \exp(Q/RT) \quad (14)$$

Table 13: Diffusion coefficients of Ag, Fe, Ni and oxygen in various host materials (in β-Zr, α-Zr, and ZrO_2).

Tracer species	Host Material	Do m^2/s	h_a J/mol	Dj (1500 K) m^2/s	Dj (1200 K) m^2/s	Literature
Oxygen	ZrO_2			≈1. E -11	≈1. E-16	[43]
Zr	ZrO_2			≈ 1.E-16	< 1.E-22	
Oxygen	ZrO_2	1.27E-9	144907	1. E -10	6. E-12	[23]
Oxygen	α-Zr(O)	3.92E-4	214148	1. 4 E- 11	2. E- 13	"
Oxygen	β-Zr	2.63E-10	118411	2.0 E -10	2. E-11	"
Fe	β-Zr	9.1E-7 7.4E-7	113000 108000	1.2 E -10 1.3 E- 10	1.3 E -11 1.5 E -11	[35]
Co	β-Zr	3.26 E -7 3.3 E -7	91400 92000	2. E -10	3. E -11	"
Ag	β-Zr	4.2 E -8 190.5E-4	132300 324400	1. E -12	7. E -14	"
Zr	β-Zr			8.E -13	1 E -13	"
Cr	β-Zr	7. E-7	142300	8. E -12	5. E -13	"
Ni	β-Zr					
Fe	α-Zr			7. E -11	3.7 E -12	[35]
Ag	α-Zr	5.1 E -7 6.8 E -5	187100 210000	1.2 E - 15	9. E -17	"
Zr	α-Zr			1. E -17	2. E -19	"
Cr	α-Zr	4.9 E -7	126000	8. E -13	1.3 E -13	"
Ni	α-Zr			9. E -11	4. E -11	"
Fe	$FeZr_3$	3.2 E -10	120000	3 E -15	4. E -16	[40]
Ni	NiZr		119000	7.6 E -13		[42]
Ni	$NiZr_2$		103000	2.1 E -13		"
Zr	Fe		103000	2.1 E -13		"
Zr	Ni		103000	2.1 E -13		"

Diffusion coefficients defined as: $\mathbf{D_{j(T)} = D_0 \cdot exp\ (-h_a / RT)}$, R= 8.314 J/mol K

Table 14: Estimated diffusion coefficients (m^2/s) for Fe, Ni in the liquid phase ([1]) of the chemical interaction (A) stainless steel 316 / Zry and (B) Inconel / Zry.

A: Estimated diffusion coefficients from reaction rates and binary phase diagram Fe-Zr

T /K	c s -	c s +	c xi -	c xi +	Delta c xi	Delta c'	Kpxi	D''(Fe)	D' Zr	D''Fe	D'eff(Zr)
1273	0,01	0,74	0,77	0,93	0,16	0,03	1,17E-11	1,3E-11	*8,3E-11*	*2,5E-12*	5,69E-11
1373	0,01	0,68	0,81	0,94	0,13	0,13	9,74E-10	5,0E-11	*2,4E-10*	*1,1E-11*	1,52E-10
1473	0,01	0,64	0,83	0,95	0,12	0,19	4,45E-08	1,2E-10	*4,4E-09*	*2,1E-11*	3,85E-09
T /K	b s -	b s +	b xi -	b xi +	Delta b s	Delta b'	Kp s	dc'/dc(s)			D'eff(Fe)
1273	0,99	0,26	0,23	0,07	0,73	0,03	5,93E-14	4,1E-02			2,50E-17
1373	0,99	0,32	0,19	0,06	0,67	0,13	6,77E-12	1,9E-01			6,37E-14
1473	0,99	0,36	0,17	0,05	0,63	0,19	4,07E-10	3,0E-01			9,25E-12

B: Estimated diffusion coefficients from reaction rates and binary phase diagram Ni-Zr

T /K	c s -	c s +	c xi -	c xi +	Delta c xi	Delta c'	Kpxi	D''(Ni)	D' Zr	D'' Ni	D'eff(Ni)
1273	0,01	0,74	0,77	0,97	0,2	0,03	2,01E-10	1,0E-11	*2,2E-09*	*2,3E-13*	2,19E-09
1373	0,02	0,68	0,78	0,98	0,2	0,1	1,14E-09	5,0E-11	*1,1E-09*	*5,0E-13*	1,09E-09
1473	0,01	0,56	0,82	0,98	0,16	0,26	3,33E-09	1,0E-10	*3,2E-10*	*1,6E-12*	2,72E-10
T /K	b s -	b s +	b xi -	b xi +	Delta b s	Delta b'	Kp s	dc'/dc(s)			D'eff(Ni)
1273	0,99	0,26	0,23	0,03	0,73	0,03	2,28E-11	4,1E-02			9,63E-15
1373	0,98	0,32	0,22	0,02	0,66	0,1	1,73E-10	1,5E-01			9,93E-13
1473	0,99	0,44	0,18	0,02	0,55	0,26	6,07E-10	4,7E-01			3,39E-11

Diffusion coefficients and reaction rates (Kp) are given in (m^2/s).
Boundary concentrations at s (c s -, c s +, b s -, b s +) and at xi (c xi -, c xi +, b xi -, b xi +) are given in atomic frations.
Boundary concentrations b, c are given at s and xi as shown in schematics on page 20.

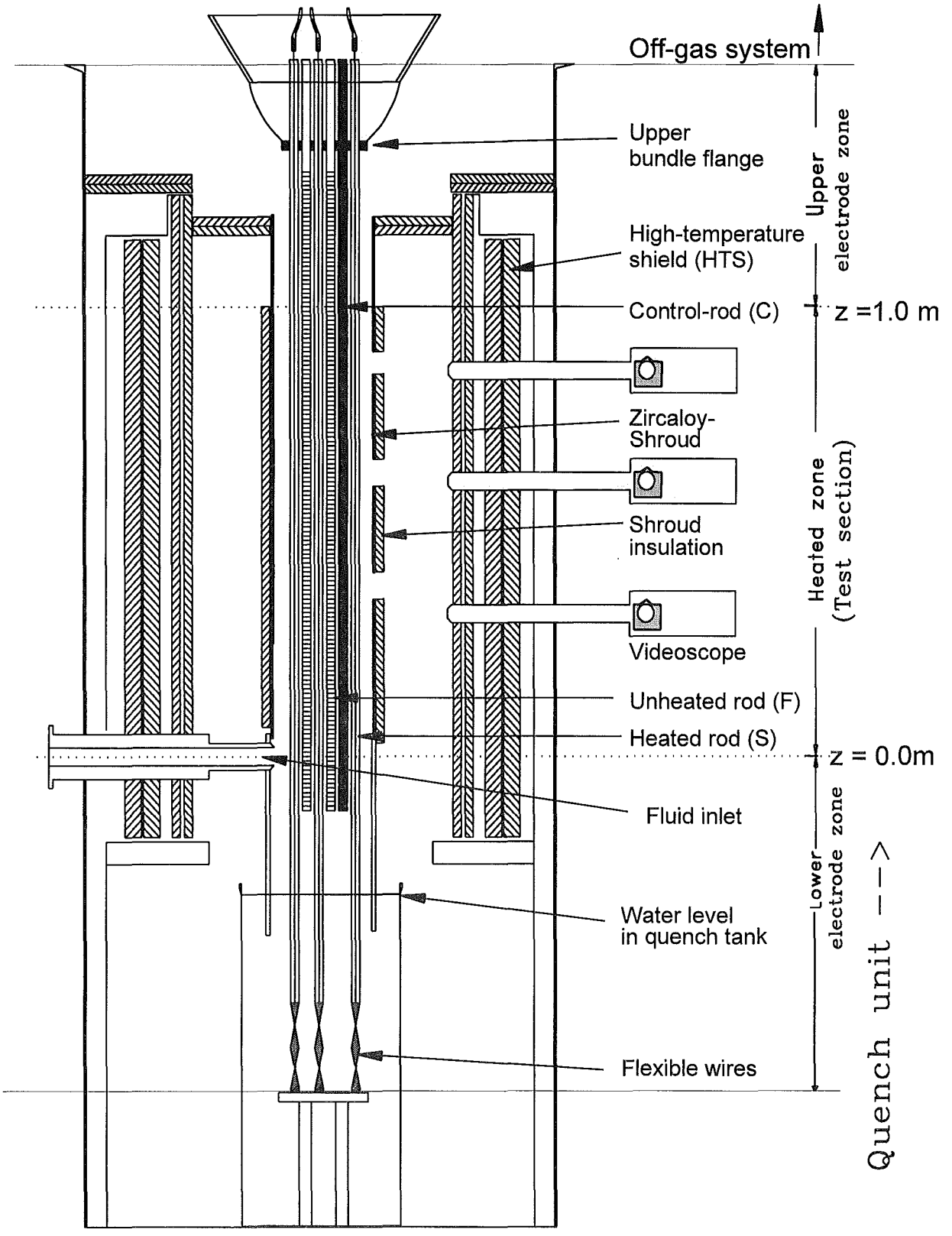

Figure 1. Schematic overview of the CORA test section: including the most important features such as fuel rod bundle, shroud with high-temperature ZrO_2 fibrin insulation, high-temperature shield (HTS) with videoscopes, and quench tank. The dotted area represents water to cool the ends of the heater rods /3/.

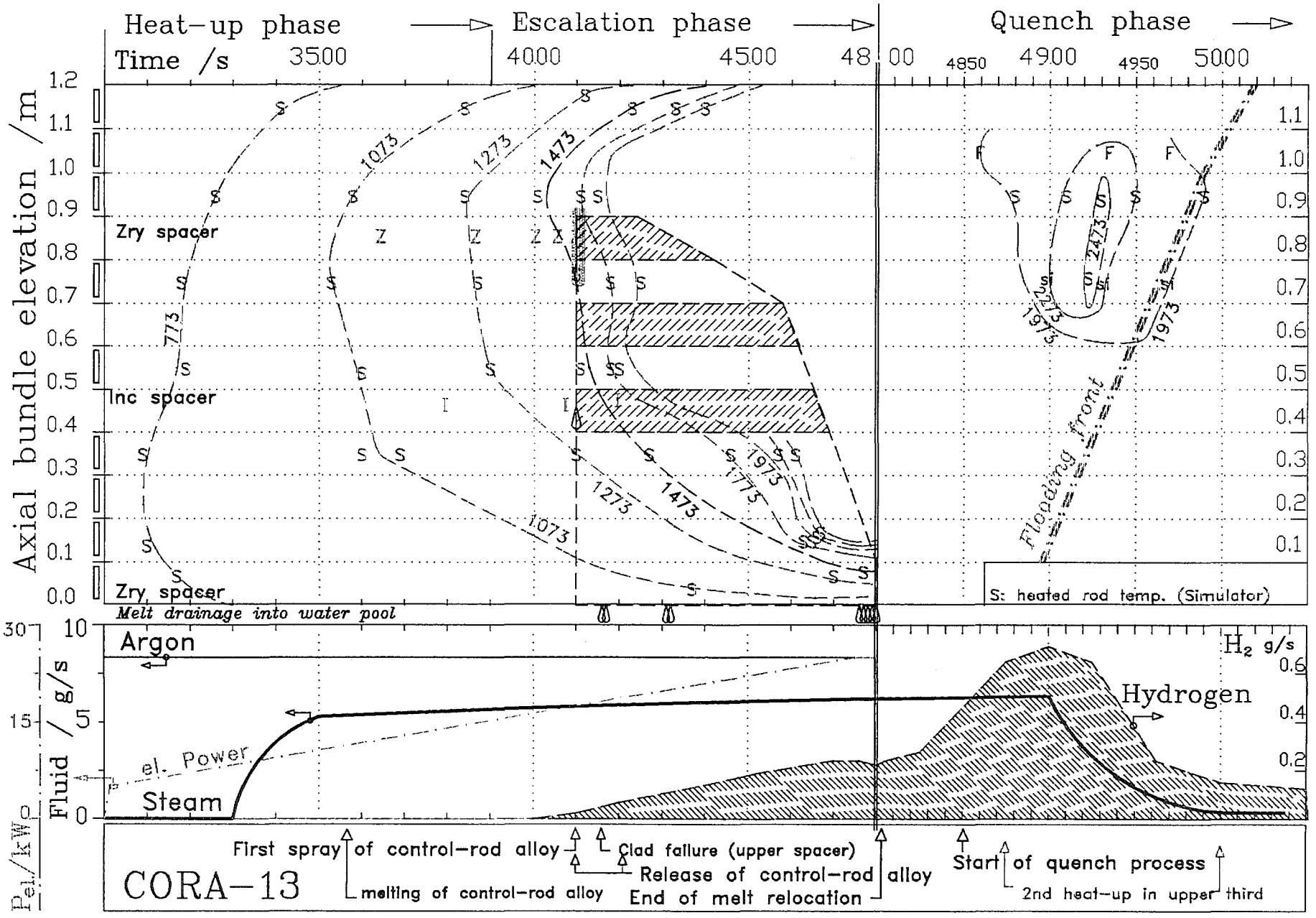

Figure 2. **Test sequence diagram of CORA-13, (ISP 31)** ***upper part:*** axial temperature front lines (TF-lines) derived from the experiment, clad failure extracted from the internal rod pressure analysis (dotted area), and melt relocation derived from the videoscope films (dashed area); ***center part:*** fluid composition at the lower end of the bundle (argon and steam), volume fraction of hydrogen in the off-gas-system and total electric power (P_{el}); ***lower part:*** identified and localized phenomena.

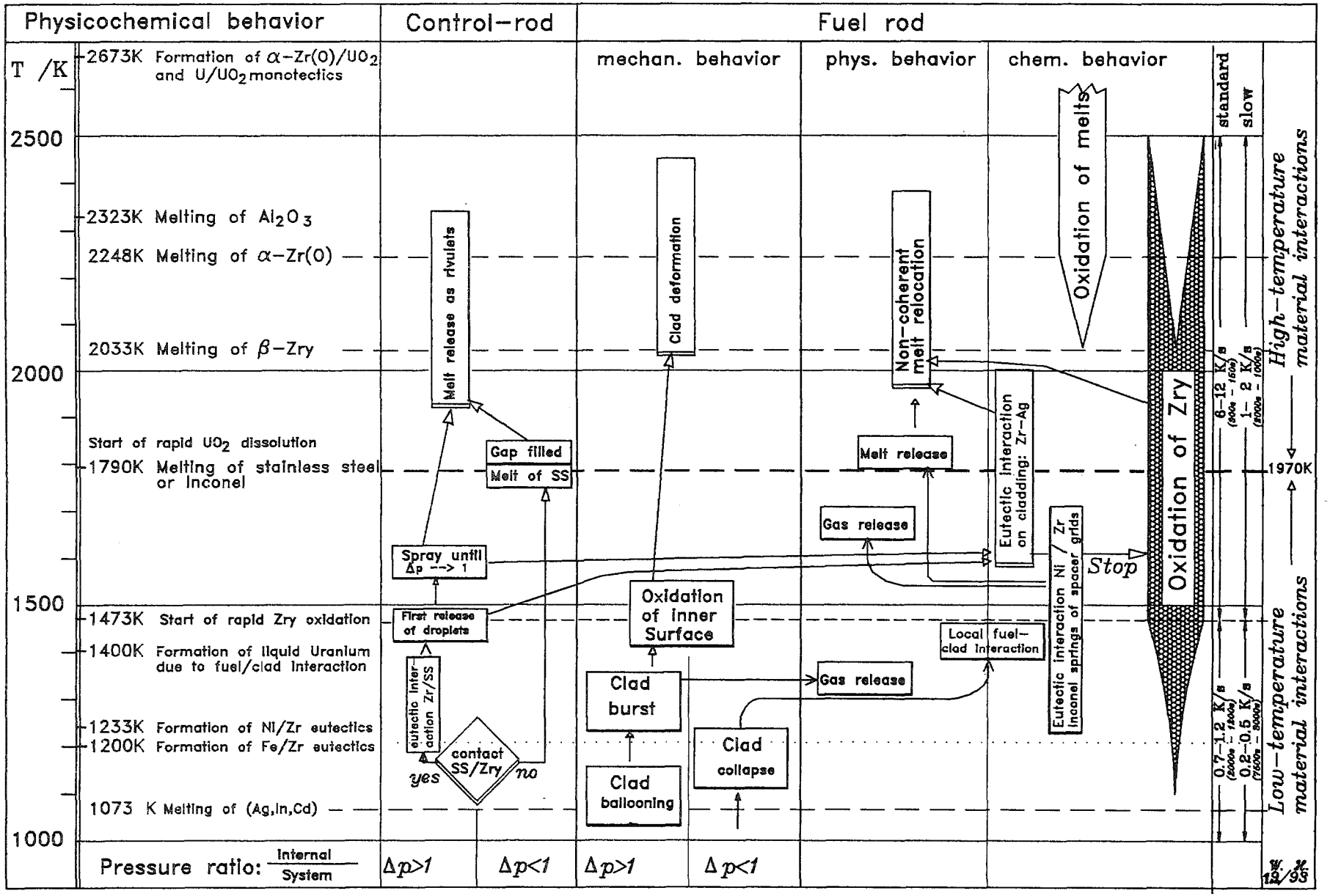

Figure 3: Chemical interactions and formation of liquid phases in a pressurised water reactor SFD accident between 1000 K and 2600 K (left side), interaction of individual processes at absorber and fuel rods (center) and time scales defined by the heat-up rates (right).

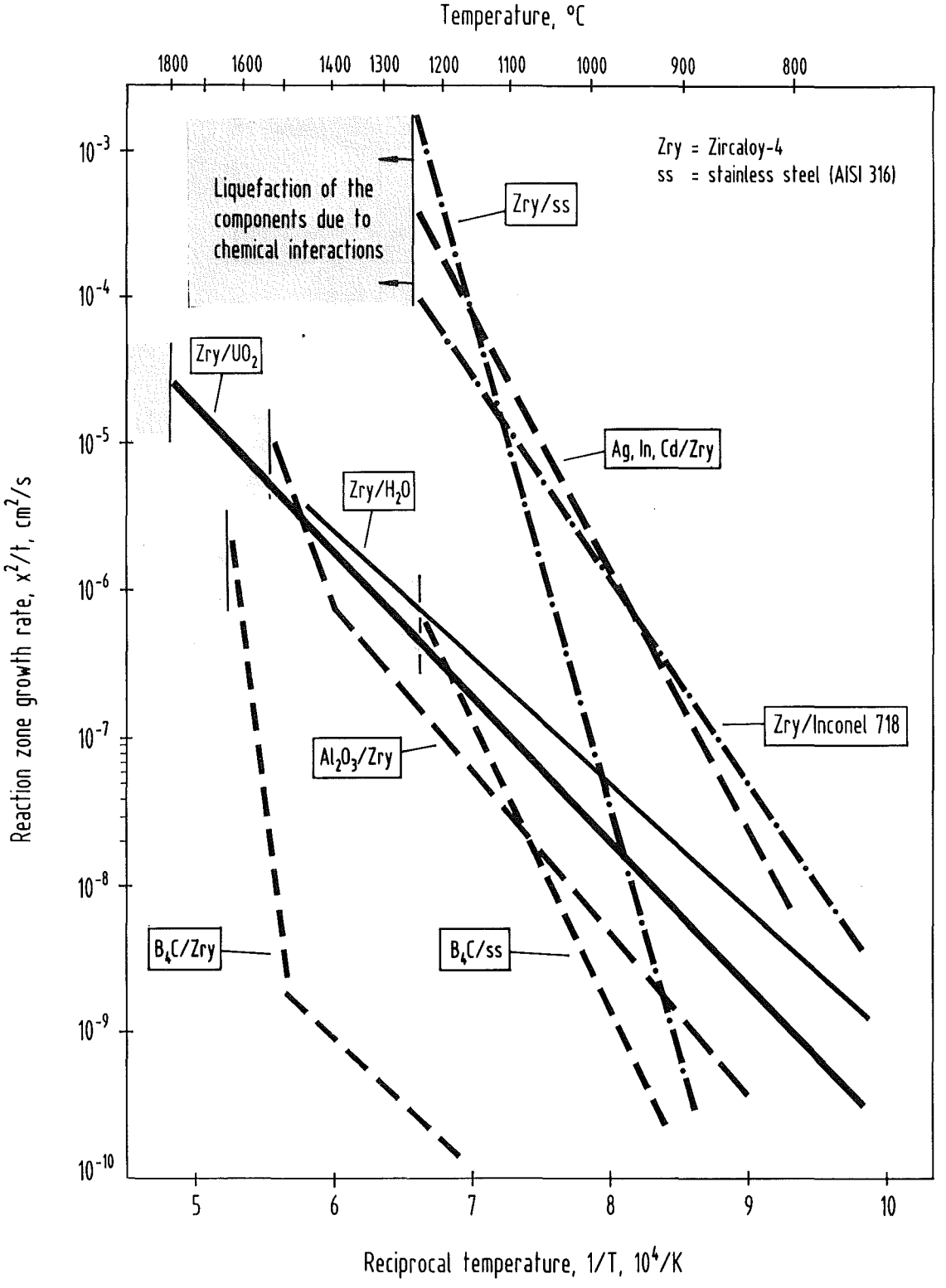

Figure 4: Reaction kinetics of chemical material interactions in the "low-temperature" and "high-temperature" region during LWR severe fuel damage accidents.

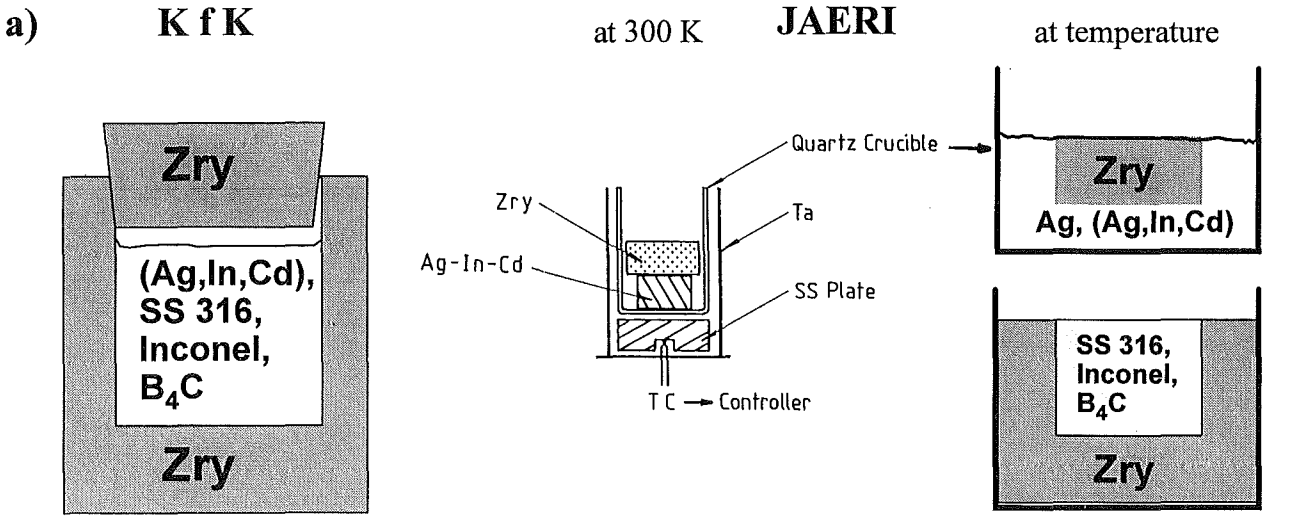

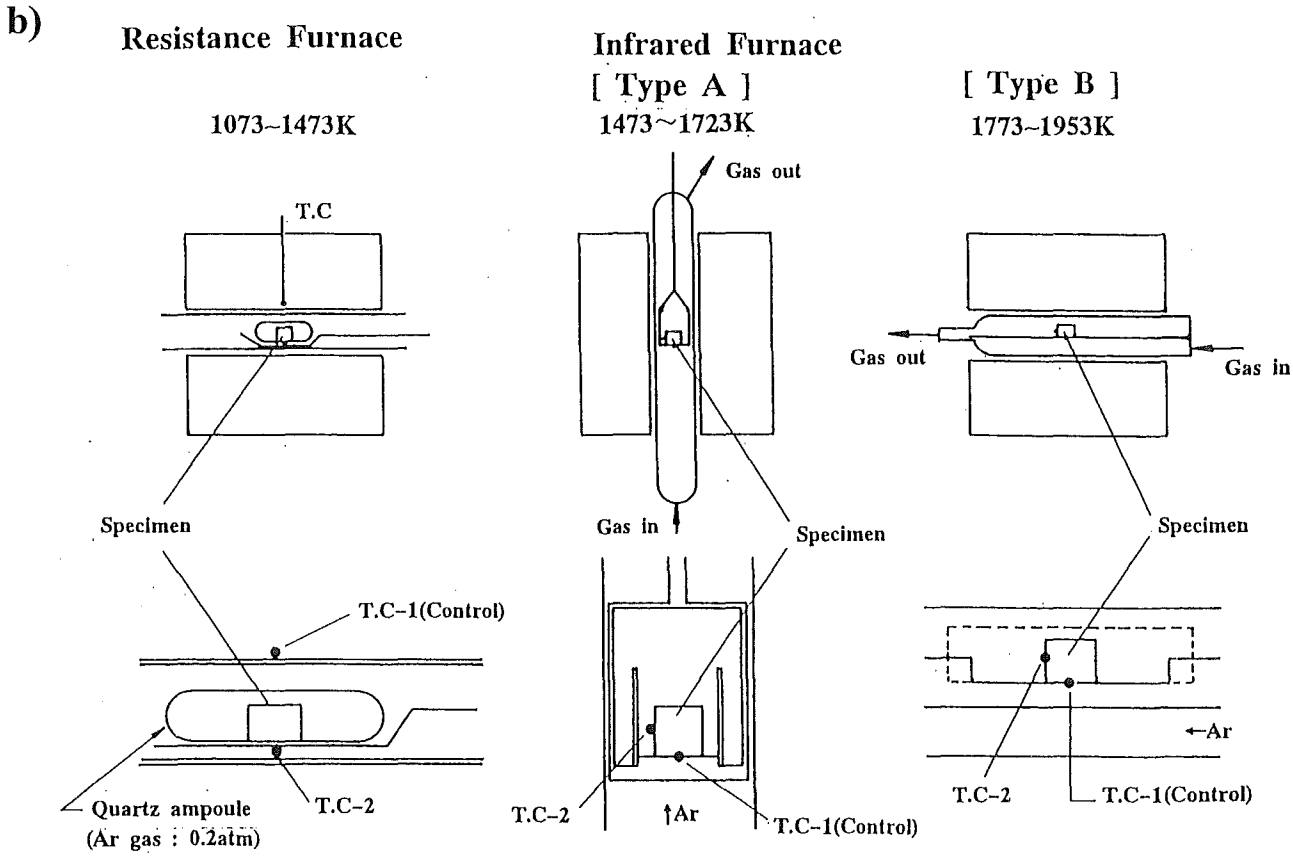

Figure 5: Test apparatus and geometry of the arrangement of specimen used for separate-effects tests: a) specimen configurations used at KfK (left) and JAERI (right), b) electric resistance and infrared furnace used at JAERI.

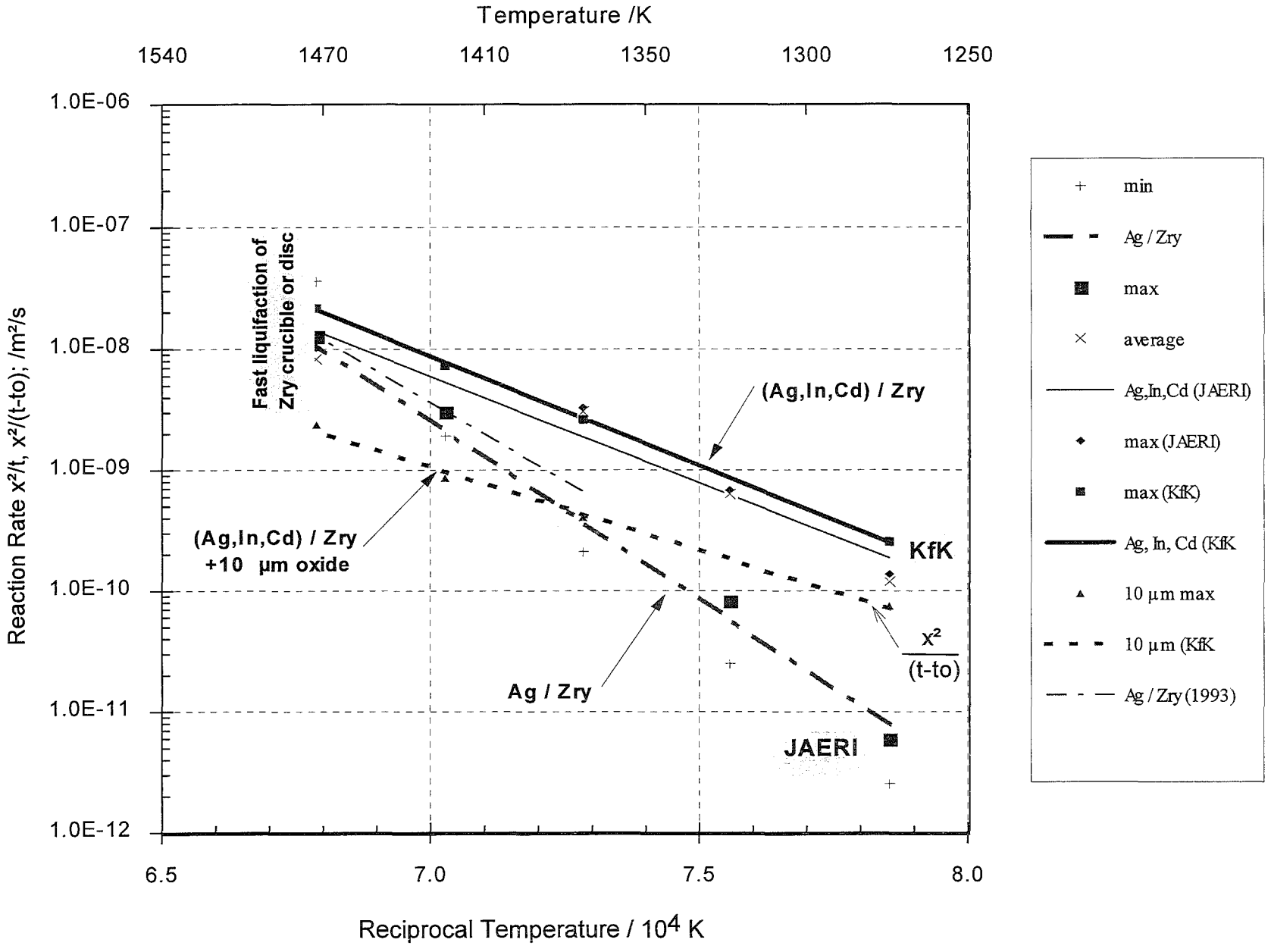

Figure 6: Measured reaction rates (x^2/t) of the chemical interaction couples with as-received Zry: Ag/Zry (JAERI) and (Ag,In,Cd)/Zry (KfK, JAERI) and with a 10 µm ZrO_2 layer pre-oxidized Zry (Ag,In,Cd)/Zry (KfK) between 1273 K and 1573 K.

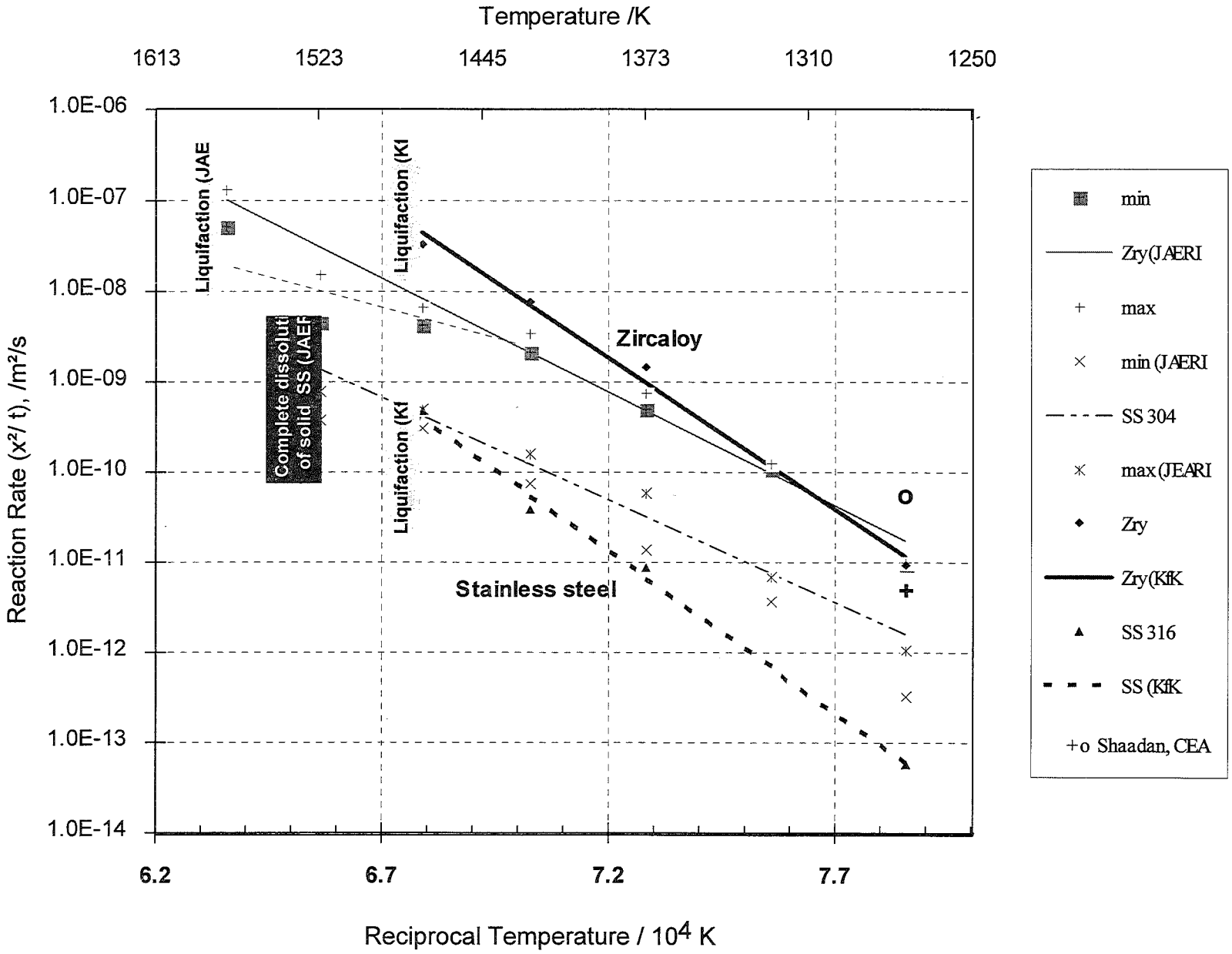

Figure 7: Measured reaction rates (x^2/t) of the chemical interaction couple stainless steel / Zry between 1273 K and 1573 K, top: reaction rate in Zircaloy, bottom: reaction rate in stainless steel.

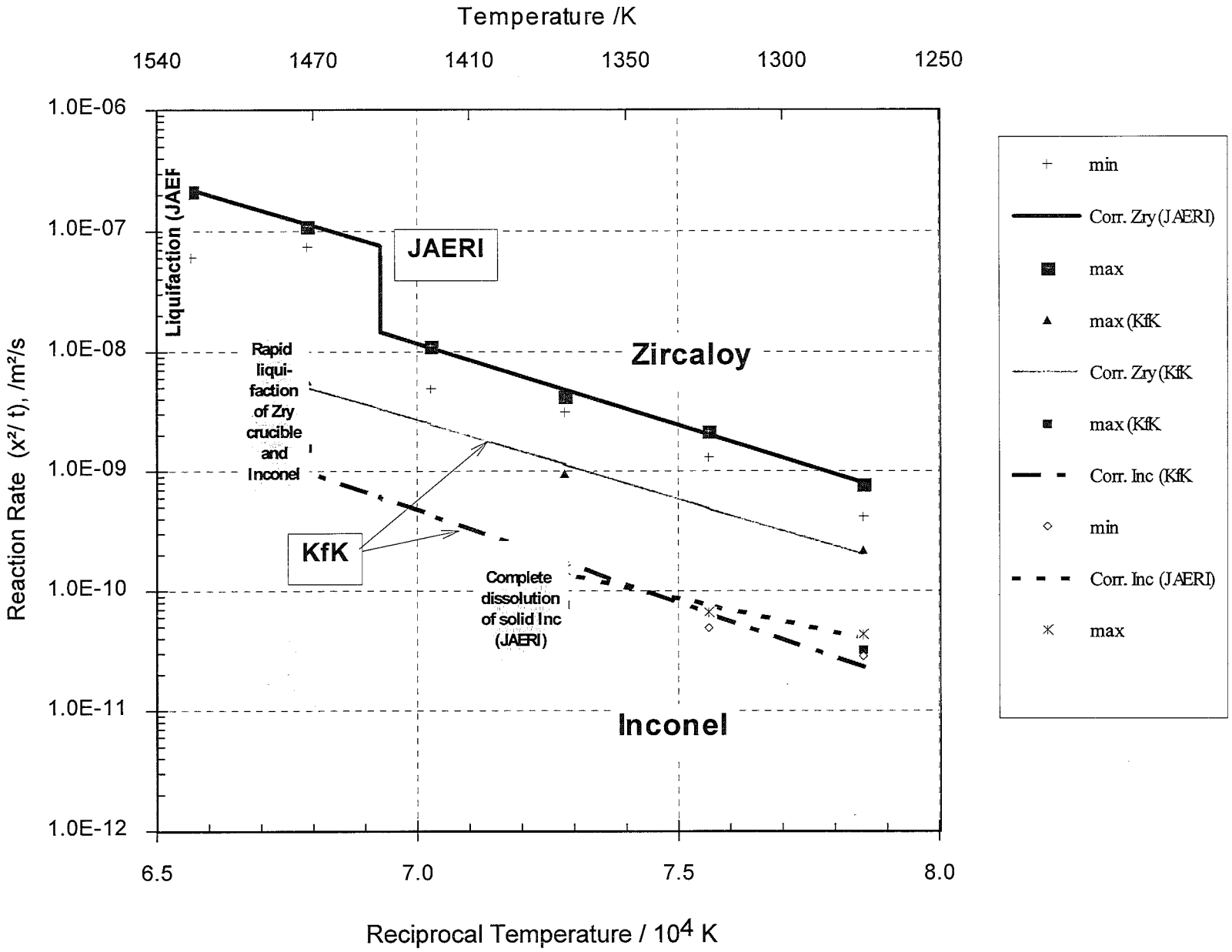

Figure 8: Measured reaction rates (x^2/t) of the chemical interaction couple Inconel / Zry between 1273 K and 1573 K solid lines: reaction rate in Zircaloy , dashed lines: reaction rate in Inconel.

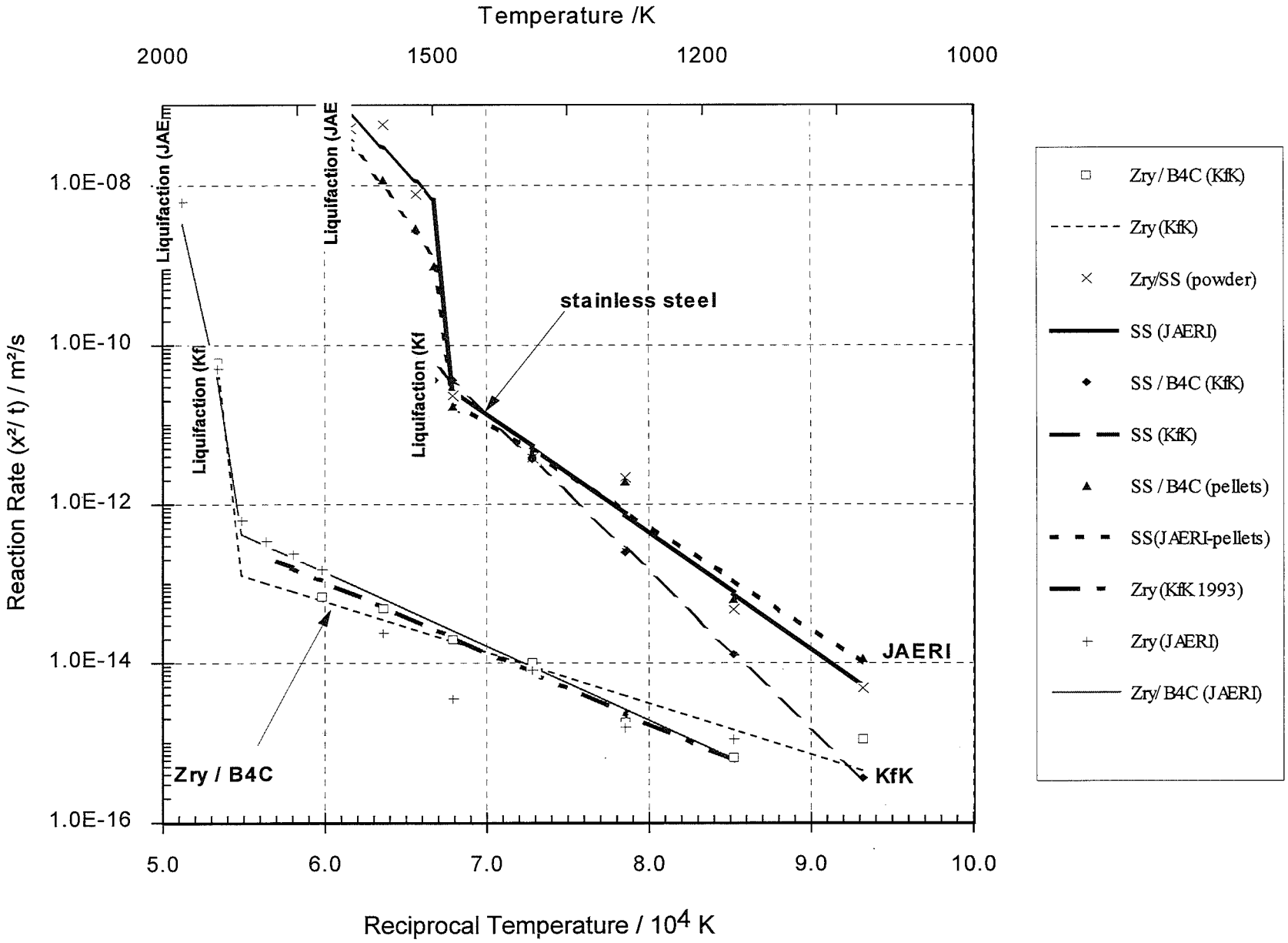

Figure 9: Measured reaction rates (x^2/t) of the chemical interaction couples: B_4C / Zry and B_4C / stainless steel, B_4C used as powder (KfK, JAERI) and pellets (JAERI) between 1273 K and 1953 K.

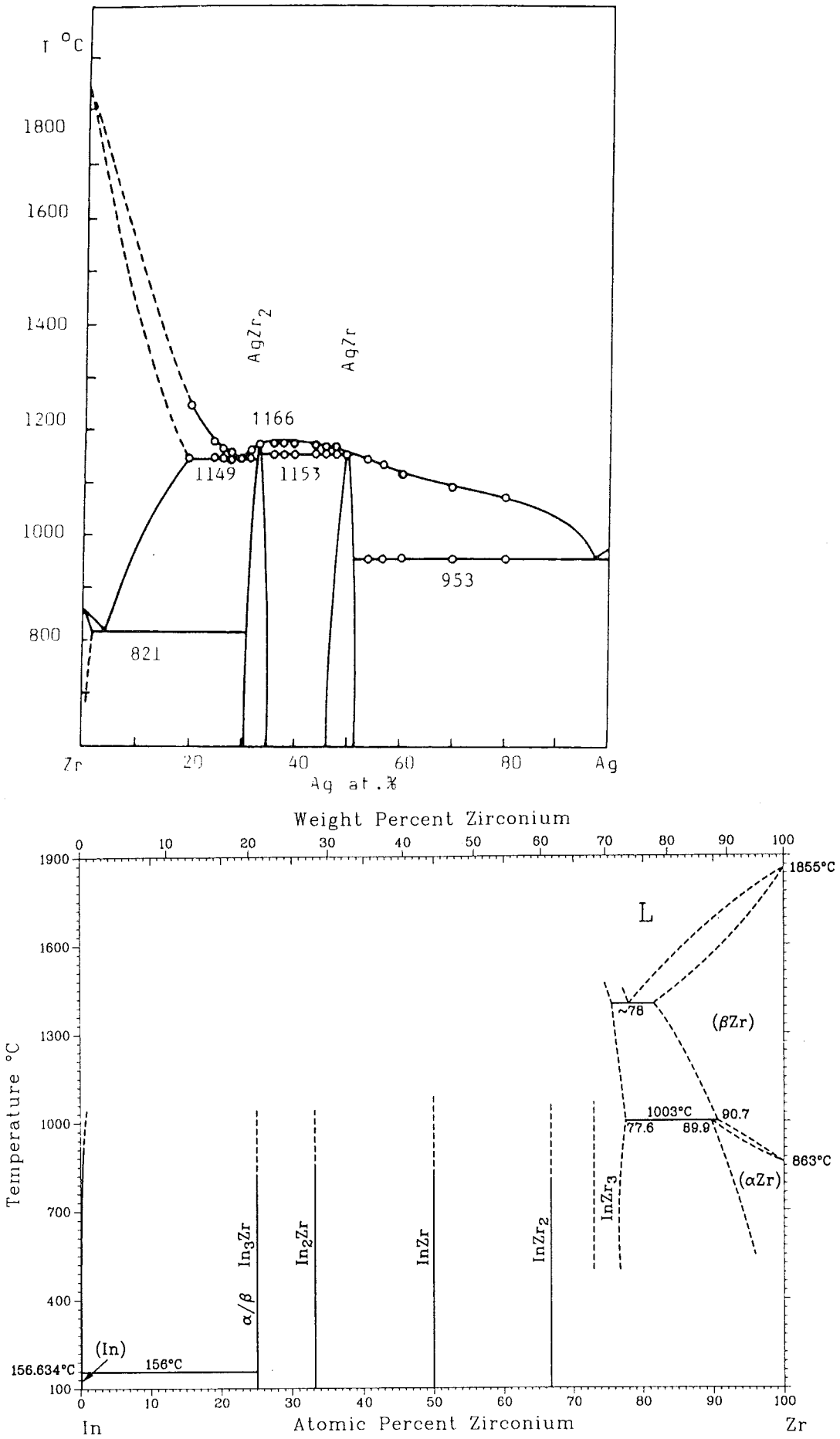

Figure 10: Binary phase diagram of Ag-Zr /11/ and In-Zr /10/ .

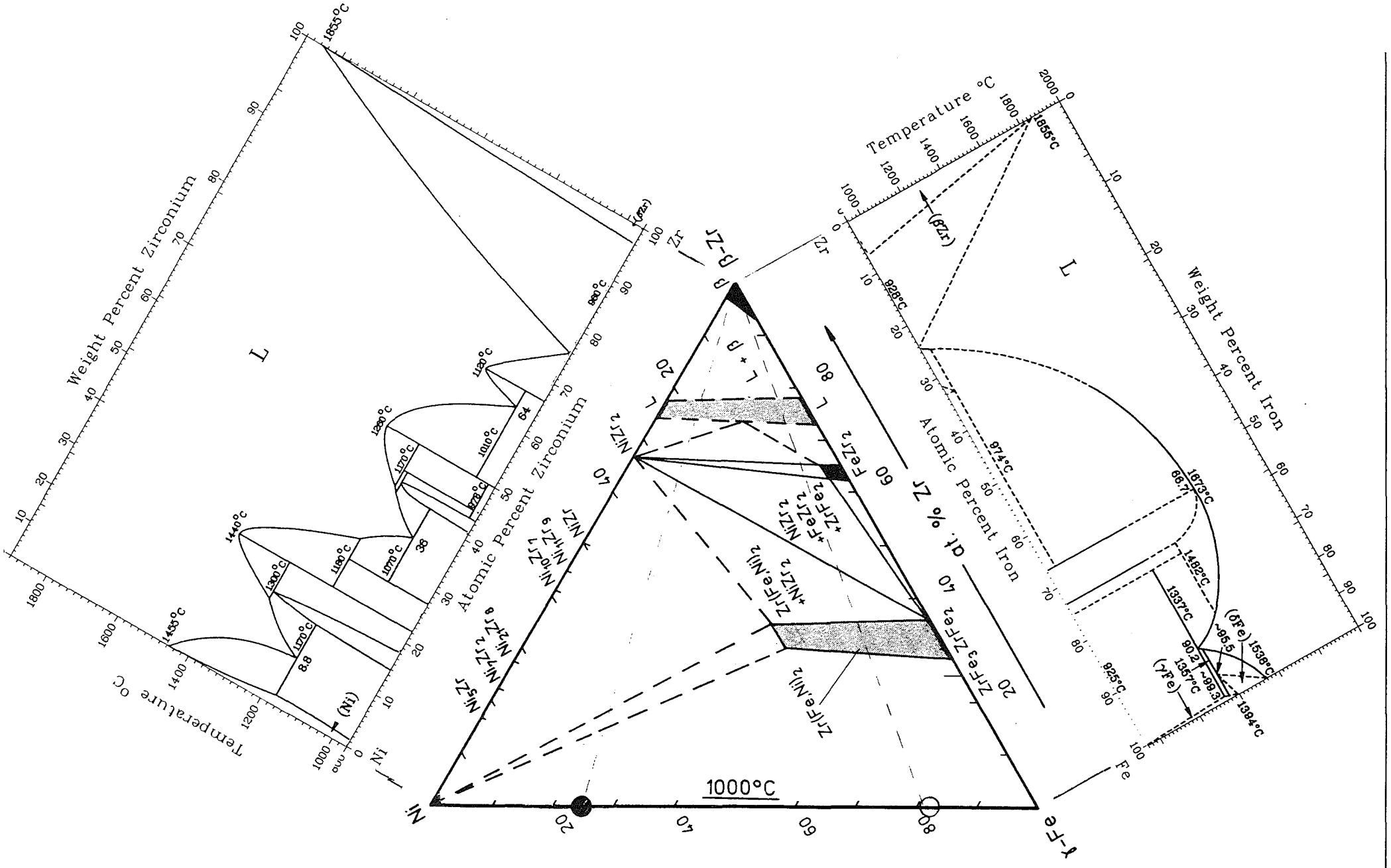

Figure 11: Isothermal section of the ternary phase diagram of Fe-Ni-Zr /8/ and the relevant binary phase diagrams Fe-Zr and Ni-Zr above 1200 K. The corresponding tie lines are given as thin dashed lines between β-Zr and stainless steel (open circle) and Inconel (solid circle).

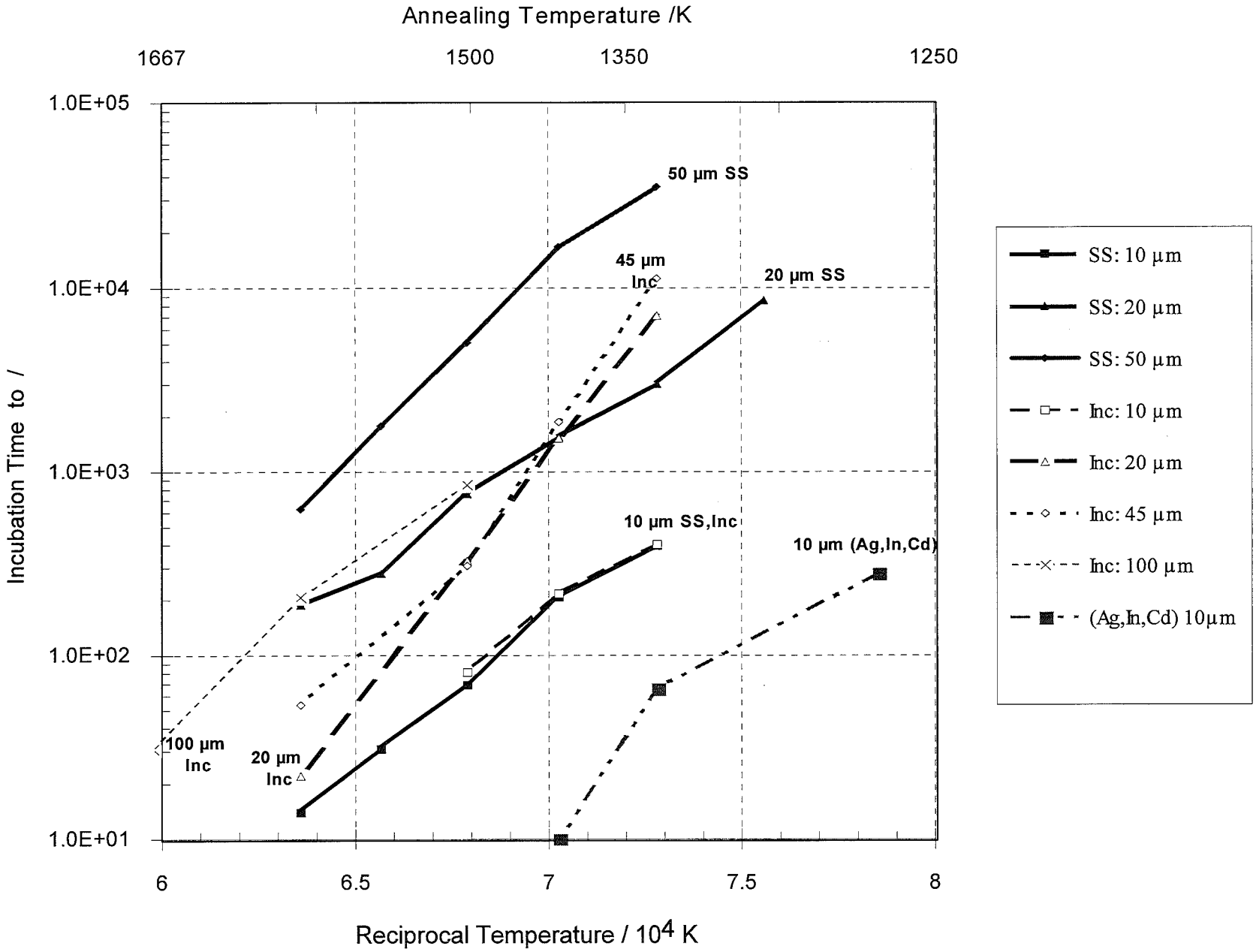

Figure 12: Isothermal section of the ternary phase diagram of Fe-Ni-Zr [8] and the relevant binary phase diagrams Fe-Zr and Ni-Zr above 1200 K. The corresponding diffusion paths between β-Zry and stainless steel (open circle) and Inconel 718 (solid circle) are marked by thin dashed lines.

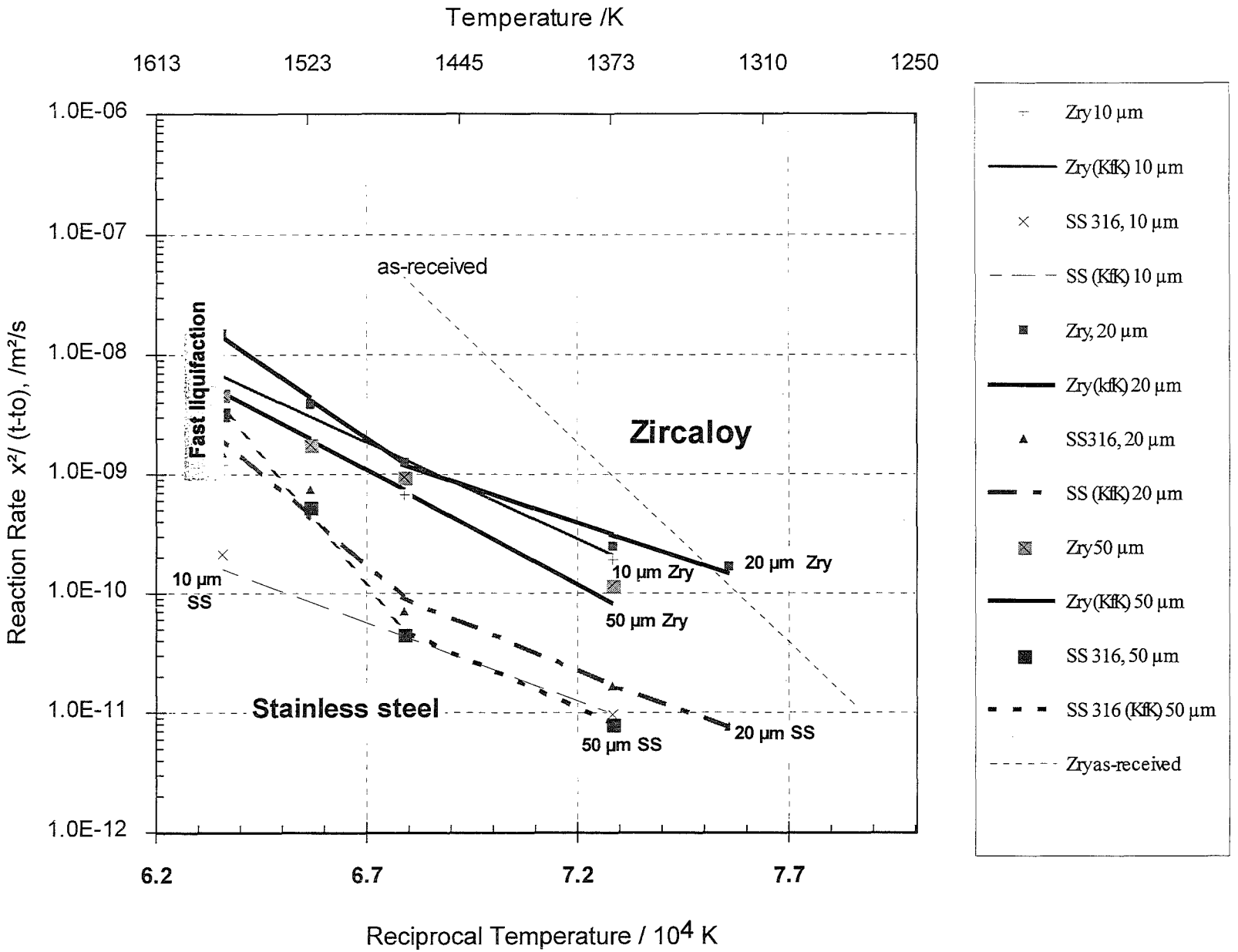

Figure 13: Measured reaction rates $x^2/(t\text{-}to)$ for various initial oxide layer thicknesses for the couple: stainless steel / Zircaloy between 1273 K and 1573 K.

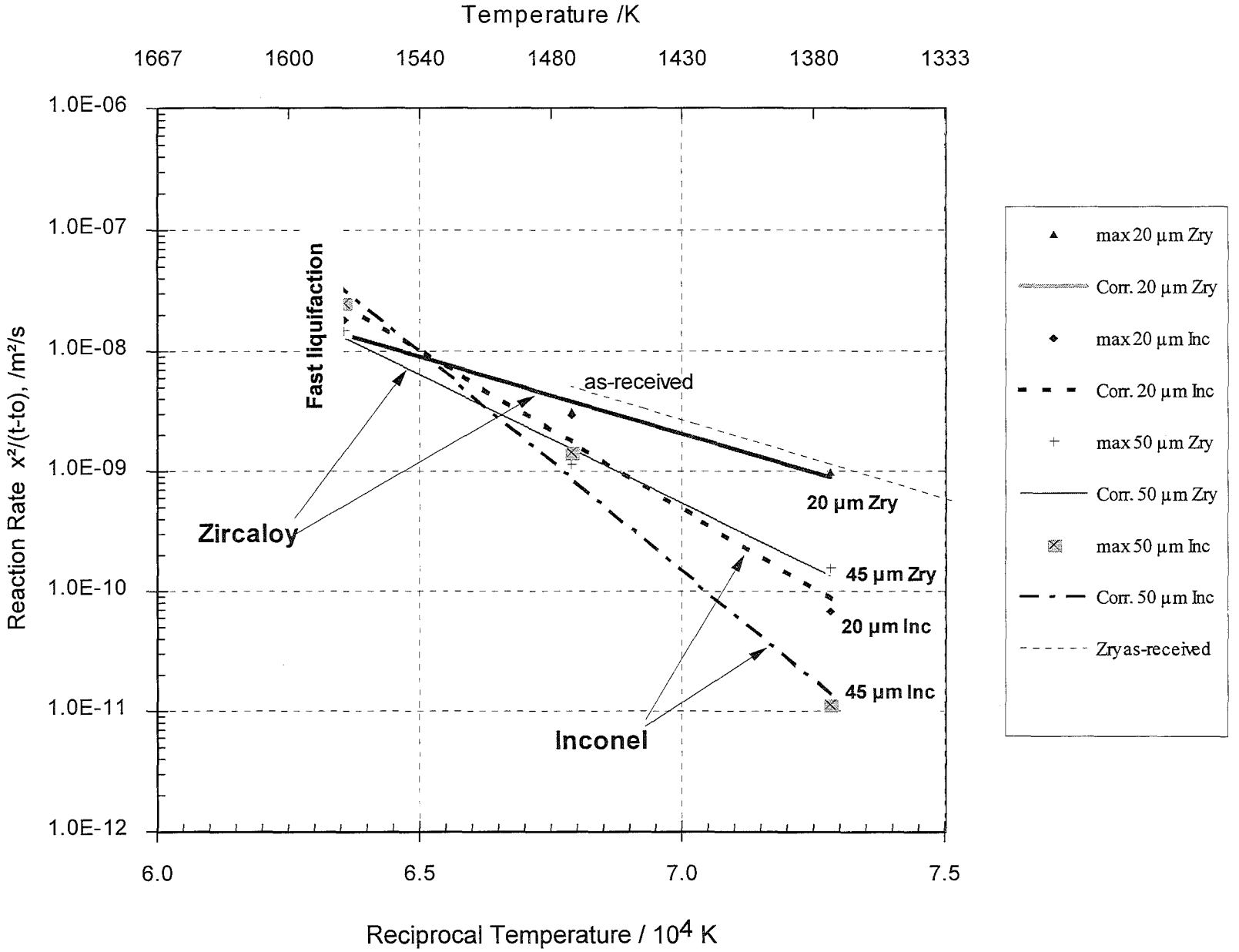

Figure 14: Measured reaction rates $x^2/(t-to)$ for various initial oxide layer thicknesses for the chemical interaction couple Inconel / Zircaloy between 1273 K and 1573 K.